Artemisinin resistance mutations in *Pfcoronin* impede hemoglobin uptake

Imran Ullah[1], Madeline A. Farringer[1], Anna Y. Burkhard[1], Erica Hathaway[2], Bailey C. Willett[1], Malhar Khushu[1], Sara H. Shin[1], Aabha I. Sharma[1], Kairon L. Shao[1], Morgan C. Martin[1], Jeffrey D. Dvorin[3], Daniel L. Hartl[4], Sarah K. Volkman[1], Selina Bopp[1], Sabrina Absalon*[2], Dyann F. Wirth*[1]

[1]Department of Immunology and Infectious Diseases, Harvard T.H. Chan School of Public Health, Boston, MA, USA.

[2]Department of Pharmacology and Toxicology, Indiana University School of Medicine, Indianapolis, IN, USA.

[3]Department of Pediatrics, Harvard Medical School, Boston, MA, USA.

[4]Department of Organismic and Evolutionary Biology, Harvard University, Boston, MA, USA.

*Corresponding authors:

Dyann F. Wirth*: dfwirth@hsph.harvard.edu

Sabrina Absalon*: sabsalon@iu.edu

Abstract

Artemisinin (ART) combination therapies have been critical in reducing malaria morbidity and mortality, but these important drugs are threatened by growing resistance associated with mutations in *Pfcoronin* and *Pfkelch13*. Here, we describe the mechanism of *Pfcoronin*-mediated ART resistance. *Pf*Coronin interacts with *Pf*Actin and localizes to membranes of the parasite periphery, the digestive vacuole (DV), and a putative pre-DV compartment (PPDC)—all structures involved in the trafficking of hemoglobin from the RBC for degradation in the DV. *Pfcoronin* mutations alter *Pf*Actin homeostasis and impair the development and morphology of the PPDC. Ultimately, these changes are associated with decreased uptake of red blood cell cytosolic contents by ring-stage *Plasmodium falciparum*. Previous work has identified decreased hemoglobin uptake as the mechanism of *Pfkelch*13-mediated ART resistance. This work demonstrates that *Pf*Coronin appears to act via a parallel pathway. For both *Pfkelch13*-mediated and *Pfcoronin*-mediated ART resistance, we hypothesize that the decreased hemoglobin uptake in ring stage parasites results in less heme-based activation of the artemisinin endoperoxide ring and reduced cytocidal activity. This study deepens our understanding of ART resistance, as well as hemoglobin uptake and development of the DV in early-stage parasites.

Introduction

Rapidly acting and potent antimalarial drugs, such as artemisinin (ART) and others in its class, are critical components of current front-line treatments, and these drugs have contributed to yearly reductions in malaria mortality for the past two decades[1]. However, partial resistance to ART and artemisinin combination therapies (ACTs) threatens their efficacy[2,3]. ART treatment failures initially emerged in Southeast Asia, and were associated with mutations in the *Plasmodium falciparum kelch13* locus[4]. The mechanism of *Pfkelch13*-mediated ART resistance is well studied, and prior work has demonstrated reduced hemoglobin uptake in ART-resistant *Pfkelch13* mutant parasites[5,6]. ART is a sesquiterpene lactone with an endoperoxide bridge that must be cleaved to potentiate antimalarial activity. Typically, this activation occurs via heme[7], likely derived via endocytosis and digestion of hemoglobin. Thus, the observed reduction in endocytosis in *Pfkelch13* mutants may decrease the availability of free heme, slowing the activation of ART and leading to ART resistance [5,6].

As part of our previous efforts to understand potential ART-resistance mechanism(s) in Africa, we demonstrated *Pfcoronin* to be a major driver of *in vitro* partial ART resistance in Senegalese isolates of *P. falciparum*[8,9]. Coronin proteins are widely conserved, and while many organisms have multiple *coronin* genes, *P. falciparum* and other unicellular pathogens encode just one[10,11]. Like other Coronin orthologs, *Pf*Coronin includes a WD40 domain. These domains are thought to facilitate protein-protein interactions and are involved in a wide range of cellular functions[12,13]. Coronin proteins have been associated with actin-binding activities in multiple organisms[14]; in the apicomplexan parasite, *Toxoplasma gondii*, *Tg*Coronin regulates the rate and extent of actin polymerization, and is required for endocytosis and recycling of membranes[15]. In *P. berghei*, *Pb*Coronin is implicated in the regulation of gliding motility in sporozoites[16]. In *P. falciparum*, *in vitro* biochemical studies have confirmed that the WD40 domain of *Pf*Coronin binds actin and organizes F-actin filaments into parallel bundles[17]. In late asexual blood-stage parasites, *Pf*Coronin localizes to the parasite periphery, potentially linking actin filaments to the plasma membrane[17]; localization in earlier stages has not been previously assessed.

Here, we study *Pf*Coronin and identify its interaction partners in both rings and late-stage parasites. Furthermore, we assess the impact of *Pfcoronin* mutations on protein levels, subcellular localization, and hemoglobin uptake to improve our understanding of potential early-stage parasite DV development and ART activation.

Results

Reduced interaction of *Pf*Coronin mutants with *Pf*Actin in rings: Previously, we demonstrated that mutations in the *Pfcoronin* gene are a major driver of *in vitro* evolved ART resistance in Senegalese isolates of *P. falciparum*, as measured by the ring-stage survival assay (RSA)[8]. Either a single G50E mutation (Senegalese isolate from Thiès) or paired R100K/E107V mutations (Senegalese isolate from Pikine) are sufficient to confer resistance[8,9]. *Pf*Coronin contains a seven-bladed WD40 domain with Gly50 located in the first blade, and both Arg100 and Glu107 located in the second blade. We focused on the Pikine *P. falciparum* isolate in this study. WD40 domains have previously been associated with the facilitation of protein-protein interactions[12,13]. Therefore, to identify interaction partners of *Pf*Coronin, we appended the spaghetti monster-human influenza hemagglutinin (HA) tag (smHA)[18] to the c-terminus of the endogenous *Pfcoronin* locus in both *Pfcoronin*^{WT} and *Pfcoronin*$^{R100K/E107V}$ genetic backgrounds (Supplementary Fig. 1). We immunoprecipitated (IP) *Pf*Coronin-smHA protein in both early ring and later trophozoite-stage parasites [3-9 or 32 – 40 hours post-invasion (hpi)] using anti-HA antibodies (Supplementary Fig. 2a); we also included an untagged *Pfcoronin*^{WT} control line. Co-purified proteins were identified by liquid chromatography with tandem mass spectrometry (LC-MS/MS). To identify potential *Pf*Coronin interacting partners, we first filtered out proteins that were found in the untagged line and normalized prey protein abundance to that of *Pf*Coronin bait abundance [(Supplementary Data 1 (3-9 hpi); Supplementary Data 2 (32 – 40 hpi)]. We established two criteria to prioritize top *Pf*Coronin interacting partners: (1) the protein must be detected in all replicates of either *Pf*Coronin^{WT}-smHA or *Pf*Coronin$^{R100K/E107V}$-smHA parasites and (2) its abundance must be at least 5% of *Pf*Coronin (bait) protein abundance. To investigate interactions that were potentially affected by mutations in *Pfcoronin*, we looked for differentially-associated proteins, for which there was a greater than 5x change in normalized abundance between *Pf*Coronin^{WT}-smHA and *Pf*Coronin$^{R100K/E107V}$-smHA, and/or for which the *p*-value (unpaired t-test between *Pf*Coronin^{WT}-smHA and *Pf*Coronin$^{R100K/E107V}$-smHA) was less than 0.05 [(Supplementary Fig. 2b and Supplementary Data 3 (3-9 hpi); Supplementary Fig. 2c and Supplementary Data 4 (32 – 40 hpi)]. Interestingly, in both stages, the major interacting partner of *Pf*Coronin was *Pf*Actin (Fig. 1a-b), consistent with its role in regulating actin dynamics. At ring stage, this interaction was reduced by three-fold in *Pf*Coronin$^{R100K/E107V}$-smHA parasites (p = 0.0113; Fig. 1a and Supplementary Fig. 2b; Supplementary Data 3); this reduction did not occur in the late-stage parasites (p = 0.4787; Fig. 1b and Supplementary Fig. 2c; Supplementary Data 4). Additionally, while polyubiquitin (*Pf*Ub) was an abundant interaction partner of *Pf*Coronin^{WT}-smHA in ring-stage parasites (3-9 hpi), its interactions with *Pf*Coronin$^{R100K/E107V}$ were dramatically reduced by 15-fold (p=0.0282; Fig. 1a and Supplementary Fig. 2b; Supplementary Data 3). In late-stage parasites, we did not observe substantial or significant changes in associations with *Pf*Ub by *Pf*Coronin^{WT}-smHA vs. *Pf*Coronin$^{R100K/E107V}$-smHA (p = 0.4493; Supplementary Fig. 2c and Supplementary Table 4).

***Pfcoronin* mutations only confer ART resistance in rings:** Overall, comparison between *Pf*Coronin interaction partners in *Pf*Coronin^{WT} vs. *Pf*Coronin$^{R100K/E107V}$ parasites showed far more differences at ring-stage than in late-stage parasites. Interestingly, this corresponds to the timing of clinical resistance to ART, which manifests as delayed clearance of early ring-stage parasites. Additionally, *Pfkelch13*-mediated ART resistance in cultured parasites is only evident at the ring stage[4,6]. As a result, the ring-stage survival assay (RSA), in which ring-stage parasites are exposed to physiological concentrations of dihydroartemisinin (DHA) for just 6 hours, has become

the standard assay for *in vitro* ART resistance, with greater than 1% survival indicating ART resistance[4]. To assess whether *Pfcoronin*-mediated ART resistance is stage-specific, we treated parasites with pulses of 700 nM DHA for 6-hour increments across development. Similarly, to *Pfkelch13* mutants, *Pfcoronin*-mediated artemisinin resistance is ring-stage specific: *Pfcoronin*$^{R100K/E107V}$ mutants did not show any resistance phenotype beyond the first 6 hours of the lifecycle (Fig. 1c).

***Pfcoronin* mutations reduce *Pf*Actin protein levels in rings:** Since we observed reduced interactions with *Pf*Actin in *Pfcoronin*$^{R100K/E107V}$ mutant ring-stage parasites, we were interested in whether these changes represented global differences in *Pf*Actin protein levels. We performed western blot analysis on ring-stage parasite lysates to assess whether *Pf*Actin abundance differs between *Pfcoronin*^{WT} and *Pfcoronin*$^{R100K/E107V}$ mutant parasites. We found that *Pfcoronin*$^{R100K/E107V}$ parasites contained 31 ± 5.8 % (mean ± SEM) less *Pf*Actin, compared to *Pfcoronin*^{WT} parasites in rings (p = 0.027; Fig. 1d; see Supplementary Fig. 3a for full western blot images and additional examples). This decrease in *Pf*Actin protein levels is consistent with the reduced interactions with *Pf*Actin in *Pfcoronin*$^{R100K/E107V}$ mutant ring-stage parasites; however, it is not clear how *Pfcoronin*$^{R100K/E107V}$ mutations mediate these changes. We did not observe changes in *Pf*Actin protein levels in late-stage parasites (Supplementary Fig. 3b).

***Pf*Actin is ubiquitinated only in *Pfcoronin*^{WT} parasites in rings:** To gain further insights into the changes associated with *Pfcoronin*$^{R100K/E107V}$ mutations, we focused on the second most abundant *Pf*Coronin interaction partner, annotated as polyubiquitin, which exhibited striking 15-fold changes in associations with *Pf*Coronin$^{R100K/E107V}$-smHA, compared to *Pf*Coronin$^{R100K/E107V\text{-}smHA}$, in ring stage parasites (Fig. 1a, Supplementary Fig. 2b; Supplementary Data 3). We questioned whether the dramatic reduction in apparent interactions with "polyubiquitin" in *Pfcoronin*$^{R100K/E107V}$ mutant ring-stage parasites represented global differences in ubiquitination or specific changes in ubiquitination of *Pf*Coronin or its interaction partners.

First, to explore overall protein ubiquitination in *Pfcoronin*^{WT}*-smHA* vs. *Pfcoronin*$^{R100K/E107V}$*-smHA* parasites, we generated ring-stage parasite lysates (3-9 hpi) and performed anti-ubiquitin Western blots. We found no noticeable difference between the *Pfcoronin*^{WT}*-smHA* and the *Pfcoronin*$^{R100K/E107V}$*-smHA* mutant (Fig. 1E; see Supplementary Fig. 4a for full western blot images and additional examples), suggesting that global changes in the ubiquitination system were unlikely. To identify potential changes in specific ubiquitinated proteins, we identified ubiquitin-interacting partners using an anti-ubiquitin antibody in *Pfcoronin*^{WT}*-smHA* and *Pfcoronin*$^{R100K/E107V}$*-smHA* ring-stage parasites (Supplementary Fig. 4b). As before, we focused on proteins that were detected in all replicates of either *Pfcoronin*^{WT}*-smHA* or *Pfcoronin*$^{R100K/E107V}$*-smHA* parasites (Supplementary Fig. 4c and Supplementary Data 5). Of these putatively-ubiquitinated proteins, only two were found to interact with *Pf*Coronin in this study (Supplementary Data 3): eukaryotic initiation factor 4A (eIF4A) and *Pf*Actin. *Pf*Actin was of particular interest because of its high abundance in anti-smHA (*Pf*Coronin) IP experiments and its known interaction with *Pf*Coronin. Interestingly, associations between *Pf*Actin and ubiquitin were detected in *Pfcoronin*^{WT}*-smHA* parasites, but not in *Pfcoronin*$^{R100K/E107V}$*-smHA* samples (Fig. 1f).

Detection of *Pf*Actin via anti-ubiquitin antibodies could indicate that *Pf*Actin itself is ubiquitinated, or that *Pf*Actin physically associates with another protein (or proteins) that is ubiquitinated. To distinguish between these possibilities, we performed Lys-ϵ-Gly-Gly (diGly) proteomics, which identifies not only which proteins are ubiquitinated, but also at which sites[19]

153 (Supplementary Fig. 5a). We identified ubiquitination events at K114 and K62 of *Pf*Actin only in
154 *Pfcoronin*^{WT} parasites (Supplementary Fig. 5b; Supplementary Data 6).

155 ***Pfcoronin* mutants sensitize *Pf*Actin to jasplakinolide:** Our data revealed that
156 *Pfcoronin*$^{R100K/E107V}$*-smHA* parasites have changes in *Pf*Actin abundance and ubiquitination. We
157 therefore hypothesized that *Pfcoronin* mutations lead to defects or dysregulation of *Pf*Actin
158 dynamics. We reasoned that these changes might alter sensitivity to jasplakinolide (JAS), which
159 stabilizes *Pf*Actin filaments and promotes polymerization, ultimately disrupting normal *Pf*Actin
160 dynamics. We tested this hypothesis using *Pfcoronin*^{WT} and *Pfcoronin*$^{R100K/E107V}$ parasites (DHA
161 selected Pikine_R line)[8]. We first estimated sensitivity to JAS using a standard 72 h growth assay
162 and found no difference between *Pfcoronin*^{WT} (EC_{50} = 40.1 ± 1.3 nM) and *Pfcoronin*$^{R100K/E107V}$
163 parasites (EC_{50} = 37 ± 2.6 nM; Fig. 1g and Supplementary Fig. 5c). To assess possible differences
164 in ring-stage parasites, we performed RSA-type assays on *Pfcoronin*^{WT} and *Pfcoronin*$^{R100K/E107V}$
165 parasites. Parasites were treated for 6 hrs, starting at 3 hpi, with 740 nM JAS (~20X EC_{50}). JAS
166 had a modest effect on *Pfcoronin*^{WT} parasite survival (84 ± 9% survival) but significantly reduced
167 the survival of *Pfcoronin*$^{R100K/E107V}$ parasites (17 ± 6 % survival) (Fig. 1h). Thus, *Pfcoronin*
168 mutations sensitize parasites to *Pf*Actin disruptions, suggesting some level of underlying *Pf*Actin
169 dysfunction or dysregulation, particularly in early ring-stage parasites.

170 ***Pf*Coronin localizes to the periphery during late schizogony:** We used immunofluorescence
171 assay (IFA) to investigate *Pf*Coronin localization. Previous IFA studies[17] have shown that
172 *Pf*Coronin is localized to the membrane of individual merozoites during late schizogony.
173 Consistent with these studies, *Pf*Coronin-smHA was localized to the merozoite membrane).
174 Potential co-localization with the major interacting partner, *Pf*Actin, was also assessed. *Pf*Actin
175 was distributed throughout the parasite (Fig. 2) and was found in close proximity to *Pf*Coronin at
176 the membrane, but its localization did not substantially overlap with *Pf*Coronin (Fig. 2). We did not
177 find any observable differences in localization of *Pf*Coronin and *Pf*Actin in WT vs. mutant late
178 stage, segmenting parasites (Fig. 2).

179 ***Pf*Coronin marks vesicular ultrastructures across development**: To gain further insights into
180 *Pf*Coronin localization, we performed ultrastructure expansion microscopy (U-ExM) imaging using
181 Airyscan2 super-resolution microscopy[20,21]. *Pf*Coronin had not previously been examined during
182 ring-stage—the most relevant stage for ART resistance. We therefore assessed *Pf*Coronin
183 localization in rings as well as throughout development (Fig. 3). *Pf*Coronin was found at the
184 membranes, likely representing the parasite plasma membrane (PPM) and/or parasite vacuolar
185 membrane (PVM) (Fig. 3). In rings (6 – 15 hpi), in addition to PPM/PVM, *Pf*Coronin is localized
186 around an intracellular vacuole that may be a precursor to the DV; we refer to this vacuole as the
187 "putative pre-DV compartment" (PPDC). The identification of PPDC-like vacuoles was first
188 observed in earlier research utilizing electron microscopy (EM)[22]. PPDC contains host
189 cytoplasmic content, predominantly hemoglobin, demonstrated by staining with NHS ester, (Fig.
190 3, rings) and further confirmed through staining of biotin-dextran (RBCs had been pre-loaded with
191 biotin-dextran; see below; Supplementary Fig. 6). Further investigation in trophozoite stage
192 parasites (26 – 34 hpi) confirmed localization of *Pf*Coronin at the DV membrane (Fig. 3).
193 Interestingly, in addition to the PPM/PVM and DV membrane, *Pf*Coronin is localized to small
194 double and single membrane-bound vacuoles (Fig. 3). These small vacuoles are located in close
195 proximity to the cytostome, but do not overlap with the cytostome (Fig. 3) nor did we observe
196 *Pf*Coronin signal at the cytostome (Fig 3). In addition, we observed *Pf*Coronin-labeled
197 interconnected chains of small and large vacuoles (Supplementary Fig. 7). IFA analysis of early

198 schizonts showed similar localization to the periphery, DV membrane, and smaller vesicles near
199 the DV (Supplementary Fig. 8).
200 ***Pf*Coronin mutations disrupt its ultrastructure localization and protein levels:** We next
201 compared localization of *Pf*Coronin^{WT}-smHA vs. *Pf*Coronin$^{R100K/E107V}$-smHA using U-ExM.
202 Interestingly, *Pf*Coronin$^{R100K/E107V}$ localizes to disorganized puncta at ring stage, but shows a WT-
203 like distribution in late schizonts (Fig. 4a; Supplementary Fig. 9). We hypothesized that the
204 disorganized punctate localization of *Pf*Coronin$^{R100K/E107V}$-smHA might be associated with reduced
205 protein levels and therefore we performed immunoblot-based quantification analysis. We found
206 significantly less *Pf*Coronin protein in the R100K/E107V mutant than in WT ring-stage parasites
207 (3-9 hpi), but protein levels were unchanged in late-stage parasites (32-40 hpi) (Fig. 4b; see
208 Supplementary Fig. 10 for full western blot images and additional examples). This result suggests
209 that *Pfcoronin* mutations result in reduced protein levels.

210 **Mutations affect the size and number of *Pf*Coronin-labelled hemoglobin-filled PPDC and**
211 **invaginations in early rings:** The *Pf*Coronin-labelled PPDC, which houses host cell cytoplasmic
212 contents, e.g., hemoglobin (Fig. 3, rings; Supplementary Fig. 6), is visible in many ring-stage
213 parasites. *Pf*Coronin is also localized around large invaginations (Fig 5a). While the PPDC
214 appears as a vacuole in older ring-stage parasites (>9hpi), invaginations are more commonly
215 observed in early rings (<9hpi; Fig 5a). In our U-ExM studies of early ring-stage parasites (0-9
216 hpi), the *PfCoronin$^{R100K/E107V}$-smHA* mutant parasites showed a significant decrease in the
217 presence of the PPDC and/or invagination, with only 23.8% of parasites displaying this feature
218 (Fisher's exact test, $p < 0.0001$; Supplementary Fig. 11a). In contrast, all analyzed images of
219 *Pfcoronin^{WT}-smHA* parasites showed the presence of the PPDC and/or invagination. We
220 measured the size of PPDC/invagination and normalized it to the parasite size for both
221 *Pfcoronin^{WT}-smHA* and *Pfcoronin$^{R100K/E107V}$-smHA* mutant parasites. We observed a 21%
222 reduction in the PPDC/invagination in *Pfcoronin$^{R100K/E107V}$-smHA* parasites (unpaired t-test; p =
223 0.0340; Fig 5b; Supplementary Fig.11b-d).
224
225 **Mutations in *Pfcoronin* reduce hemoglobin uptake:** Prior studies demonstrated that the uptake
226 of RBC contents is decreased in ART-resistant *Pfkelch13* mutants[5,6]. This reduction in
227 endocytosis may slow the activation of ART by decreasing the availability of free heme.
228 Localization of *Pf*Coronin to the membranes of the parasite periphery, vesicular structures,
229 including internalized PPDC and invaginations, and DV—all structures involved in the trafficking
230 of hemoglobin from the RBC to the DV—suggested that *Pf*Coronin, similarly to *Pf*Kelch13, may
231 play a role in the uptake of hemoglobin and other RBC contents. To test this hypothesis, we
232 performed a previously published microscopy-based endocytosis assay, which uses fluorescein-
233 dextran as a tracer for uptake of host cell contents[5]. Fluorescein-dextran-loaded RBCs were
234 mixed with late schizonts and incubated for 3 hours to allow invasion. After 3 hours, the remaining
235 schizonts were removed by sorbitol synchronization. The resulting population of 0-3 hpi parasites
236 were allowed to grow within the fluorescein-dextran-loaded RBCs for 6 hours. Following this
237 incubation, RBC cell contents were removed with saponin, leaving just the young parasites, which
238 were fixed. Image analyses were performed as previously described[5] (Supplementary Fig. 12a-
239 b). Since *Pfkelch13^{C580Y}* mutants had previously been assessed in the same assay[6], we used
240 *Pfkelch13-3D7^{C580Y}* mutants[9] to validate the assay. We measured a significant 35% reduction in
241 fluorescein-dextran uptake in *Pfkelch13^{C580Y}* mutant parasites compared to the *Pikine^{WT}* parent
242 (unpaired Mann-Whitney test; $p < 0.0001$; Supplementary Fig. 13a; see supplementary Fig. 15
243 for individual bioreps). This figure closely matches the 37.47% reduction previously reported in
244 *Pfkelch13-3D7^{C580Y}* mutants[5]. We then assessed fluorescein-dextran uptake in *Pfcoronin$^{R100K/E107V}$*

245 mutants. Interestingly, we observed a 21.3% reduction in fluorescein-dextran uptake in
246 *Pfcoronin*$^{R100K/E107V}$ mutants compared to WT parasites (unpaired Mann-Whitney test; $p < 0.0001$;
247 Fig. 5c). Resolution was insufficient to determine whether fluorescein-dextran was contained in
248 fully-internalized vacuoles or in membrane invaginations, but analysis revealed that dextran-
249 containing compartments in *Pfcoronin*$^{R100K/E107V}$ mutants were significantly smaller compared to
250 those in WT parasites (unpaired Mann-Whitney test; $p < 0.0001$; Fig. 5d). *Pfkelch13*^{C580Y} mutants
251 exhibited a 4.9% decrease in vesicle size compared to WT parasites (Supplementary Fig. 13b).
252 Integrated density analyses, considering both intensity and vesicle size, revealed a 45.5%
253 reduction in *Pfcoronin*$^{R100K/E107V}$ mutants (unpaired Mann-Whitney test; $p < 0.0001$; Fig. 5e) and
254 37.1% reduction in *Pfkelch13* mutants (unpaired Mann-Whitney test; $p < 0.0001$; Supplementary
255 Fig. 13c). Notably, fluorescein-dextran-containing compartments were not seen in all parasites;
256 the above analyses only considered parasites in which fluorescein-dextran-containing
257 compartments were observed. To further investigate differences in the presence or absence of
258 endocytosed fluorescein-dextran, we assessed the numbers of WT vs. mutant parasites in which
259 any fluorescence was visible. We found a significant difference (Chi-square, Baptista-Pike test; p
260 < 0.0001); endocytosis had occurred in 72% of WT parasites, but only 46% of mutants (Fig. 5f;
261 Supplementary Fig. 16). In summary, our findings reveal that both *Pfcoronin* and *Pfkelch13* alter
262 endocytosis and reduce hemoglobin uptake to mediate ART resistance. However, the unique
263 localization of *Pf*Coronin to the parasite membrane, PPDC, invagination, and the DV membrane,
264 along with its impact on the number and size of invaginations, suggests that *Pf*Coronin facilitates
265 hemoglobin uptake through a different mechanism.

266

Discussion

In this manuscript, we provide insights into the molecular mechanism of *Pfcoronin*-mediated ART resistance. We demonstrate that *Pfcoronin* mutations confer ART resistance only in early ring-stage parasites. In line with the ring-stage specific phenotype, associations of *Pf*Coronin with the two major interacting partners, *Pf*Actin and polyubiquitin, are significantly reduced in *Pfcoronin* mutants at ring stage, but not at later stages. Additionally, *Pf*Actin protein levels are reduced in ring-stage *Pfcoronin*$^{R100K/E107V}$ mutants, compared to *Pfcoronin*^{WT} parasites, and ring-stage *Pfcoronin*$^{R100K/E107V}$ mutants are sensitized to killing by JAS, which promotes actin polymerization. U-ExM revealed that *Pf*Coronin is localized to the associated with the parasite membrane and the DV membrane, as well as a previously-undescribed putative pre-DC compartment (PPDC) and hemoglobin-filled invaginations in ring-stage parasites. Mutations in *Pfcoronin* alter the number and size of these invaginations. Finally, we found that *Pfcoronin* mutations significantly reduce uptake of RBC contents. Similar reductions in hemoglobin uptake have been associated with *Pfkelch13*-mediated ART resistance[5].

We present multiple lines of evidence indicating that mutations in *Pfcoronin* impact *Pf*Coronin protein levels, its subcellular localization, and homeostasis of *Pf*Actin—the major interacting partner of *Pf*Coronin—in ring-stage parasites. Actin filament polymerization and decay enable the formation of specialized structures and drive multiple complex cellular processes such as vesicular trafficking and endocytosis[23]. In *P. falciparum,* dysregulation of *Pf*Actin using the filament stabilizing agent, JAS, alters cytostome morphology and inhibits hemoglobin trafficking to the DV[24]. We find that mutations in *Pfcoronin* alter the regulation of *Pf*Actin, including changes in quantity and in ubiquitination status. These findings are consistent with a previous study in *P. chabaudi*, where actin was among one of three proteins identified to be ubiquitinated in ring-stage parasites[25]. Studies in other organisms have also reported ubiquitination of actin[26], and ubiquitin has been shown to play a role in actin homeostasis[27]. In *Pfcoronin*$^{R100K/E107V}$ mutants, it is unclear whether the observed changes in *Pf*Actin quantity, ubiquitination, some other aspect of interactions with *Pf*Coronin, or a combination thereof, is most important in altering *Pf*Actin dynamics and driving ART resistance. However, these changes in *Pf*Actin dynamics are underlined by the hypersensitivity of *Pfcoronin*$^{R100K/E107V}$ mutant parasites to JAS treatment.

Despite the importance of endocytosis and vesicular trafficking for parasite growth, the proteins and processes involved in endocytosis in *P. falciparum* are still being elucidated, with a very limited repertoire of proteins implicated[5,28–31]. In addition to *Pf*Kelch13 and its interaction partners, these proteins include phosphoinositide-binding protein PX1[32], VPS45[29], and the host enzyme peroxiredoxin 6[30]. In model organisms, actin assembly, disassembly, and turnover generate the force for membrane invagination and vesicle scission[33,34]. This process is accompanied by a host of actin regulatory proteins that work in concert to regulate actin dynamics. Only a few canonical actin-regulating proteins are maintained in *P. falciparum*[35–38]; *Pf*Coronin is one such regulatory protein.

Several genes involved in ART resistance have been implicated in hemoglobin uptake[4,39] and digestion[40]. The most-studied ART resistance gene is *Pfkelch13*[4]; mutations in *Pfkelch13* confer ART resistance by reducing *Pf*Kelch13 protein abundance. *Pfkelch13* is localized to the cytostome neck and interacts with various proteins, including *Pf*UBP1 and AP2-μ that were implicated in ART resistance in separate studies[5,39]. Disruption of *Pfkelch13* or its interaction partners, in most cases, causes both defects in endocytosis (of RBC contents) and resistance to

ART[5]. The endocytic and vesicular trafficking pathways in *P. falciparum* are not yet well-characterized, but some differences from the mammalian pathways have already surfaced. Notably, the cytostome appears to be devoid of clathrin, which mediates the most well-understood pathway for endocytosis in model organisms. On the other hand, AP2-μ, which typically works as part of the clathrin system, was observed[5]. Distinctions between mammalian and parasite processes may provide opportunities for novel drug-targeting strategies.

Prior studies on *Pf*Kelch13 showed that it is localized to the neck of the cytostome and facilitates hemoglobin uptake. The current study shows that *Pf*Coronin also facilitates hemoglobin uptake, but is localized to other structures, including the parasite membrane, DV membrane, additional small vesicles, PPDC, and/or membrane invaginations (Fig. 6). Coronin lacks any obvious post-translational lipidation motifs or a transmembrane domain, but likely associates with membranes through interaction with phosphatidylinositol 4,5-bisphosphate (PI(4,5)P2)[41]. Associations between *Pf*Kelch13 and *Pf*Coronin were not detected in this study or in a prior study on *Pf*Kelch13[5]. It therefore seems likely that *Pf*Kelch13 and *Pf*Coronin contribute to separate steps of the same endocytosis process, or function in parallel endocytic processes. These possibilities are consistent with our previous *in vitro* genetic studies, which demonstrated epistasis between *Pfcoronin*$^{R100K/E107V}$ and *Pfkelch13*^{C580Y} mutations in the Pikine genetic background[9].

There is a massive gap in knowledge regarding the uptake and processing of hemoglobin, as well as the formation of the DV. DV formation is believed to rely on *de novo* biogenesis after invasion, and the DV is not visible in early stages[22,24,42,43]. A previous study in *P. falciparum*[22] first identified a large hemoglobin-containing vacuole during the initial ring stage[22]. Another study[43], using transmission electron tomography, described a somewhat similar large vacuole-like structure, but said that it remains connected to the RBC (i.e. an invagination) throughout the entire development of the ring stage (12-24 hpi). However, a separate transmission electron tomography of the ring stage of *P. chabaudi* observed both a single large hemoglobin-containing structure, entirely contained within the parasite, and multiple small hemozoin-filled vacuoles in ring-stage parasites. This study suggested that hemoglobin uptake in the ring stage parasites is mediated via both structures, while hemoglobin uptake is completely cytostome-mediated in later trophozoite stages[44].

Recent advances in microscopy, such as U-ExM, simultaneously preserve molecular details and improve spatial resolution, allowing for a more detailed examination of ultrastructures in *P. falciparum*[20,21]. This technique is particularly advantageous in examinations of early rings, which are very small. Our U-ExM studies highlighted a large *Pf*Coronin-labeled vacuole, or PPDC, which is entirely contained within the parasite in older rings (> 9hpi), while early rings (< 9hpi) have invagination structures connected to the RBC cytosol. We did not observe additional smaller vesicles at this stage but cannot rule out the possibility that these vesicles may exist, since small vesicles could be difficult to observe using U-ExM, especially if they were not *Pf*Coronin-labeled. However, we do observe small *Pf*Coronin-labeled vesicles in trophozoites and schizonts.

The possibility of multiple hemoglobin uptake pathways, via small vs. large vesicles, as described by Wendt et al[44]. is intriguing. This possibility would be consistent with our theory that *Pfcoronin* and *Pfkelch13* regulate two separate uptake processes—only the single large vacuole is *Pf*Coronin-labeled in early rings. PPDC morphology is perturbed in *Pfcoronin* mutant parasites, suggesting that *Pf*Coronin—likely via *Pf*Actin regulation—is involved in formation of this structure. Further studies are needed to precisely delineate the process of DV formation and hemoglobin uptake in the ring-stage parasites, as well as the specific roles of *Pf*Coronin and *Pf*Kelch13.

ART remains a crucial component of front-line antimalarial therapies, and its antimalarial efficacy must be protected. The current study underlines the potential threat of *Pfcoronin*-mediated resistance—in fact, the *Pfcoronin*^{R100K} mutation was recently reported in Kenya,

359 although artemisinin sensitivity/resistance was not assessed[45]. Other *Pfcoronin* polymorphisms
360 were recently identified in Uganda[46], and these polymorphisms were associated with ART
361 resistance. We expect that surveillance of the *Pfcoronin* locus, in addition to *Pfkelch13*, will help
362 protect malaria control efforts and guide decision-making to curtail the spread of drug resistance
363 in Africa. Additionally, we hope that mechanistic understanding of *Pfcoronin*-mediated ART
364 resistance will inform strategies to defend the efficacy of ART therapies.

365

Methods

Parasite culture: *P. falciparum* culture-adapted field isolates, Pikine (SenP019.04), Pikine_R (DHA selected line[8], used for Jasplakinolide RSAs), CRISPR-engineered Pikine *Pfcoronin*$^{R100K/E107V}$ mutant (CRISPR-edited, used for timecourse experiments), *Pf*kelch13-3D7^{C580Y} mutant (CRISPR-edited, used for endocytosis)[8,9], spaghetti monster HA tag (smHA)-tagged Pikine *Pfcoronin*^{WT}*-smHA*, and Pikine *Pfcoronin*$^{R100K/E107V}$*-smHA* mutant lines (used for all experiments unless specified otherwise) were maintained in complete RPMI 1640 medium (Gibco) supplemented with 10% O^+ serum at 4% hematocrit (unless specified otherwise) in an atmosphere of 1% O2, 5% CO2, and 94% N2 at 37 °C[8,9]. All smHA-tagged lines were additionally cultured with 5nM WR99210 (Jacobus Pharmaceutical). Staging and parasitemia were assessed by light microscopy of Giemsa-stained thin blood smears[47,48]. The parasites were synchronized using sequential sorbitol lysis treatment [49].

Generation of smHA-tagged parasites and transfection: *Pfcoronin* (PF3D7_1251200) was tagged with smHA using CRISPR/Cas9. The CRISPR guide sequence (selected using benchling.com) was 5'-AATGTGTAAAAGTACAGCAA-3', which matches a site near the C-terminus of the *Pf*Coronin coding sequence. A double-stranded DNA segment with "sticky ends" was generated by annealing oligonucleotides 5'-ATTGAATGTGTAAAAGTACAGCAA-3' and 5'-AAACTTGCTGTACTTTTACACATT-3'. This segment was ligated within the U6 cassette of pBAM203[50] (pre-digested with BbsI; kind gift of Jeffrey Dvorin), proximal to the invariable part of the chimeric sgRNA scaffold, to generate pUF1-Cas9-hDHODH-Coronin. The donor/homologous repair plasmid for smHA-tagging PfCoronin was derived from pSAB55[21] (kind gift of Jeffrey Dvorin), which contains coding sequence for spaghetti monster-HA tag (smHA), followed by the *Pf*HSP86 3' UTR. Additionally, the plasmid includes a cassette for expression of human dihydrofolate reductase (hDHFR), allowing selection using WR99210. A 5' homology arm (plus shield mutations) was amplified from the end (C-terminus) of the *Pf*Coronin coding sequence using primers: 5'-CAATTGCCATGGGACAGTTTACCAAAAAATTTACCTTC-3' and 5'-ATCTCGAGTAAAACGGTTGCAGTACTTTTACACATTTTCATGTCTAG-3'; the second primer includes shield mutations to protect from cutting by Cas9. This segment was inserted into the NcoI/XhoI sites of pSAB55. A 3' homology arm was amplified from the *Pf*Coronin 3' UTR using 5'-CGTCAGGATCATCGCGGCCGCGGCACATCAGCGATCAC-3' and 5'-CATGGCAATTGAGATCTCCGAAAAATTTGTATGATATTGAAAAG-3'; this segment was inserted into the NotI/BglII sites of the plasmid using Gibson cloning, generating pSAB55-Coronin-smHA. Prior to transfection, the complete pSAB55-Coronin-smHA plasmid was linearized by digestion with NcoI. Plasmids (50 µg each of pUF1-Cas9-hDHODH-Coronin and linearized pSAB55-Coronin-smHA) were transfected into Pikine parasites carrying either *Pf*Coronin^{WT} (WT) or *Pf*Coronin$^{R100K/E107V}$, as reported previously[9]. Transfections were performed as described previously[9,51]. Transfected parasites were allowed to recover overnight before the addition of 5 nM WR99210 (selection agent for pSAB55-Coronin-smHA) and 500 nM DSM1 (selection agent for pUF1-Cas9-hDHODH-Coronin). Drug selection with DSM1 was continued for 3 days. Parasites grew up around 3 weeks and were cloned by limiting dilutions prior to studies. Confirmation of the smHA-tagged parasites is detailed in Supplementary Fig. 1.

Ring stage survival assay (RSA): RSA was performed as described previously[8,9,52,53]. *P. falciparum* cultures at the late segmented schizont stage were purified using the Percoll gradient and allowed to reinvade for 3 hours before subjecting them to synchronization. Highly

synchronized (0-3 hours post-invasion) parasites were pulsed with 700 nM DHA (Sigma-Aldrich) or 740 nM jasplakinolide (ref no, 420127, Sigma-Aldrich), or DMSO control. The pulse was followed by drug washout and further incubation at 37˚C for 66 hours, and parasitemia was assessed by light microscopy of Giemsa-stained thin blood smears[8,9]. RSA survival rates in percentage were estimated by comparing the survival of viable parasites to the untreated DMSO control for the same parasite line. Smears were blinded, and 10,000 RBCs were counted for each condition. Unless otherwise specified, all experiments used at least three independent biological replicates and two technical replicates.

Concentration–response assays: All EC_{50}s were estimated using the standard 72 hour Malaria SYBR green I fluorescence assay[54,55]. Ring-stage parasites (40 µL, 1% hematocrit and 1% starting parasitemia, n = 3) were cultured for 72 hours at 37°C in a 384-well black clear-bottom plates containing 12-point serial dilutions of test compounds, 10 µM DHA kill-control and no drug growth-control. Lysis buffer containing 16% w/v saponin, 1.6% Triton X-100, 5 mM EDTA, 20 mM Tris-HCl, pH 7.4) and 1x SYBR Green I fluorescent dye (CAT. No. S7563, Invitrogen) was added, and the plates were incubated at room temperature in the dark for at least 6 hours prior to reading. The fluorescent signal was measured using SpectraMax M5 (Molecular Devices, Sunnyvale, CA) plate reader (excitation at 494 nm, emission at 530 nm). Experiments were carried out as three technical triplicates on the same plate, with three independent biological repeats of each plate performed. Controls in each biological replicate consisted of parasite culture with no drug added (100%) or 10 µM DHA kill-control (0%). The mean and SD of fluorescence data from three independent biological repeats were expressed as a proportion of the untreated control (100%) and calculated as follows: $100 \times [\mu(S) - \mu(-)/\mu(+) - \mu(-)]$, where $\mu(S)$, $\mu(+)$ and $\mu(-)$ represent the means for the sample in question and 100% and 0% controls, respectively as previously described[48,56]. The percentage growth was plotted against $\log_{10}$-transformed drug concentration and EC_{50}s were estimated using a non-linear regression (log(inhibitor) vs response-variable slope with four parameters) in GraphPad Prism (GraphPad Software, Inc., San Diego, CA, USA). Values from the three biological replicates were used to calculate the mean EC_{50} values ± SE shown.

Co-Immunoprecipitation: For co-immunoprecipitation, (Co-IP) experiments, tightly synchronized (with 5% D-sorbitol[49] and density centrifugation with Percoll) parasites were used. A total of 4×10^9 (32 to 40 hpi, for late stages) or 4×10^9 (3-9 hpi, for ring stages) parasites were harvested by washing with PBS, and then the RBCs were lysed with 0.05% saponin in PBS in the presence of EDTA-free complete mini protease inhibitors (CAT. No. 4693159001, Sigma). The samples were then washed with PBS supplemented with protease inhibitors cocktail to remove residual RBC material. Parasite extracts were lysed in RIPA buffer (50 mM Tris-HCl, pH 7.5, 150 mM NaCl, 1% NP-40, 0.5% sodium deoxycholate, 0.1% sodium dodecyl sulfate, and EDTA-free complete mini protease inhibitors) by incubating the samples on a rotator for 1 hour at room temperature. The samples were then sonicated three times at 20% amplitude for 30 s at 4 °C with 3-minute rests on ice to chill the samples. The soluble fractions were collected by spinning the samples 12,000 g for 30 minutes and incubated with 40 µL anti-HA magnetic beads (ref no 88836, Pierce) overnight at 4 °C. For co-IP with anti-ubiquitin mAb FK2 antibody (ref no ST1200, sigma), the soluble fractions were incubated with the antibody overnight at 4 °C and then applied to protein A/G magnetic beads (CAT. No. 88802, Pierce) for 1 hour at room temperature, following the manufacturer's instructions. Beads were washed three times with RIPA in the presence of protease inhibitor cocktail, each time with a 10-minute incubation at RT on a rotator. The beads were subsequently washed once each with buffer 1 (2% SDS in dH_2O), buffer 2 (50 mM HEPES,

460 pH 7.5, 500 mM NaCl, 1 mM EDTA, 1% Triton-X 100 and 0.1% sodium deoxycholate in dH_2O)
461 and buffer 3 (10 mM Tris-HCl pH 8.0, 250 mM lithium chloride, 1 mM EDTA, 0.5% NP-40 and
462 0.5% sodium deoxycholate in dH_2O). The beads were then washed at least six times with buffer
463 4 (50 mM ammonium bicarbonate in dH_20), and resuspended in 40 µL of 5 mM ammonium
464 bicarbonate. Then, 200 ng/µL of modified sequencing-grade trypsin (Promega, Madison, WI) was
465 spiked in and the samples were incubated overnight at 37 °C. The samples were then placed on
466 a magnetic plate, and the liquid was removed. The extracts were then dried in a speed-vac (~1
467 hour). Samples were then re-suspended in 50 µL of high-performance liquid chromatography
468 (HPLC) solvent-A (2.5% acetonitrile, 0.1% formic acid) and desalted by STAGE tip[57]. On the day
469 of analysis, the samples were reconstituted in 10 µL of HPLC solvent-A. A nano-scale reverse-
470 phase HPLC capillary column was created by packing 2.6 µm C18 spherical silica beads into a
471 fused silica capillary (100 µm inner diameter, ~30 cm length) with a flame-drawn tip[58]. After
472 equilibrating the column, each sample was loaded via a Famos autosampler (LC Packings, San
473 Francisco CA) onto the column. A gradient was formed, and peptides were eluted with increasing
474 concentrations of solvent-B (97.5% acetonitrile, 0.1% formic acid). As peptides eluted, they were
475 subjected to electrospray ionization and then entered into an LTQ Orbitrap Velos Elite ion-trap
476 mass spectrometer (Thermo Fisher Scientific, Waltham, MA). Peptides were detected, isolated,
477 and fragmented to produce a tandem mass spectrum of specific fragment ions for each peptide.
478 Peptide sequences (and hence protein identity) were determined by matching protein databases
479 with the acquired fragmentation pattern by the software program, Sequest (Thermo Fisher
480 Scientific, Waltham, MA)[59]. All databases include a reversed version of all the sequences and the
481 data was filtered to between a one and two percent peptide false discovery rate.
482
483 **diGLY remnant purification and identification by LC-MS/MS:** Synchronized parasites (3-9 hpi)
484 were isolated as described previously[19], using 0.015% saponin, on ice, for 10 minutes. Following
485 washes, parasite pellets were stored at -20 °C. Samples were then prepared using the PTMScan
486 HS Ubiquitin Kit from Cell Signaling Technology (Cat. No. 59322). Following lysis, protein
487 concentrations were measured using the BCA assay (Thermo Cat. No. 23225) and lysates were
488 normalized to 5 mg/mL protein. The sample preparation was then completed according to the
489 manufacturer's instructions. Peptides were then dissolved in solvent-A, separated over a C18
490 capillary column, ionized by electrospray, and identified using an LTQ Oribtrap Velos Elite ion-
491 trap mass spectrometer (see coimmunoprecipitation, above).
492
493 **Immunoblotting:** Synchronized parasites were isolated on ice for 10 minutes with 0.015 %
494 saponin. Isolated parasites were washed three times with ice-cold PBS containing a protease
495 inhibitor cocktail (Roche cOmplete mini, Sigma Cat. No. 11836153001) before lysis in 1x Laemmli
496 Sample Buffer (Biorad Cat. No. 1610747) containing 5% beta-mercaptoethanol, followed by
497 heating the samples at 99°C for 10 minutes. Protein samples were separated on Mini-
498 PROTEAN® TGX™ Precast Gels (4–20% gradient, BioRad Cat. No. 4561091) in Tris-SDS-
499 glycine buffer. Separated proteins were transferred to a nitrocellulose membrane (Life
500 Technologies Cat. No. IB3010-31) using an iBlot system (Life Technologies). The membrane was
501 blocked in Intercept® (TBS) Blocking Buffer (LI-COR Biosciences Cat. No. 927-60001) for 1 hour
502 at room temperature on an orbital shaker. Membrane-bound proteins were first probed with
503 primary antibodies [mouse anti-*Pf*Actin 5H3 (1:100; Walter and Eliza Hall Institute of Medical
504 Research Cat. No. 26/11-5H3-1-2)[60], mouse anti-HA (1:2000; Pierce Cat. No. 26183), mouse
505 anti-ubiquitin mAb (FK2) (1:1000; Sigma Cat. No. ST1200), or rabbit polyclonal anti-BiP (1:5000;
506 kindly gifted by Jeffrey Dvorin, Harvard Medical School)] in Intercept® (TBS) with 0.2% Tween 20
507 at 4 °C overnight. The membranes were then incubated for 45 minutes at room temperature with
508 secondary antibodies [IRDye® 680RD goat anti-mouse (1:10,000; LI-COR Biosciences Cat No.
509 926-68070) and IRDye® 800CW Goat anti-Rabbit (1:10,000; LI-COR Biosciences Cat. No. 926-

510 32211)], washed, and imaged, then analyzed using the LI-COR Odyssey CLx Imager System (LI-
511 COR Biosciences).
512
513 **Microscopy-based endocytosis assay (ring-stage):** RBCs were suspended in a hypotonic
514 solution and pre-loaded with fluorescein-dextran (ThermoFisher Cat. No. D22910) as previously
515 described[6,29]. After resealing red blood cells (RBCs) and trapping fluorescein dextran within,
516 schizonts were added and allowed to re-invade by following the RSA setup. As the parasites
517 (rings) grew within the fluorescein-dextran-containing RBCs, fluorescein-dextran was
518 endocytosed and accumulated in the DV or other compartments. The parasites were then treated
519 with 5% sorbitol to remove any remaining schizonts, closely mimicking the RSA setup. Parasites
520 were washed once with RPMI medium and released from the RBCs using 10 pellet volumes of
521 PBS containing 0.015% saponin. Following 3 washes with RPMI medium, parasite samples were
522 fixed with pre-warmed 4% paraformaldehyde-0.1% glutaraldehyde in PBS for 20 minutes at 37°C.
523 Afterwards, 2-5 µL samples were loaded onto clear slides, covered with a coverslip, and allowed
524 to settle for up to 15 minutes at room temperature before imaging. DIC and AF488 channel images
525 were captured using a 100X oil immersion objective on a Zeiss Axio Observer. AF488 channel
526 images were acquired at 480 ms across all samples, with a laser intensity of 40%. Images were
527 blinded prior to analysis. Analysis was conducted for regions of interest (ROIs) where an RBC
528 ghost could be visualized around a green channel signal in the merged image. A global threshold
529 was set on 8-bit images of the green channel across images taken at the same exposure settings.
530 Area, mean gray value, and integrated density of the parasite-specific green-channel signal were
531 measured using ImageJ (https://imagej.net/ij/).
532
533 **Coverslip IFA of late-stage parasites:** Late-stage parasites were settled on to a poly-D-lysine
534 coated #1.5 12 mm coverslip for 30 minutes. After removing the supernatant, the parasites were
535 fixed with 4% paraformaldehyde for 10 minutes, then washed 3 times in PBS. Cells were
536 permeabilized with 0.1% Triton X-100 in PBS for 10 min and washed three times in PBS for 3 min.
537 Blocking solution (3% (w/v) BSA in PBS) was added and samples were incubated overnight at
538 4 °C. Primary antibodies were diluted in blocking solution and added to the coverslips for 2 hours
539 at room temperature. Coverslips were washed 3 times for 3 minutes in PBS and then incubated
540 with secondary antibody in blocking solution for 45 minutes. Coverslips were washed three times
541 with PBS, then mounted onto a slide with VectaShield Vibrance with DAPI. Parasites were
542 visualized on a Zeiss LSM980 with Airyscan2 for super-resolution microscopy. A 63x objective
543 with a numerical aperture of 1.4 was used. Dilutions for primary antibodies were 1:200 for rat anti-
544 HA and 1:300 for rabbit anti-*Pf*Actin.
545
546 **Ultrastructure Expansion Microcopy (U-ExM):** Late segmented schizont stage *Pf*Coronin^{WT}-
547 smHA or *Pf*Coronin$^{R100K/E107V}$-smHA parasites were purified by Percoll gradient centrifugation.
548 Various age groups of parasites, as specified in the Results section, were utilized for U-ExM. For
549 experiments aimed at confirming RBC content uptake, RBCs in a hypotonic solution were pre-
550 loaded with biotin-dextran (ThermoFisher Cat. No. D1956), as described in the endocytosis assay
551 above. The samples were treated with pre-warmed 4% paraformaldehyde-0.1% glutaraldehyde
552 in PBS for 20 minutes at 37 °C and prepared for U-ExM following the procedure described
553 previously[20,21]. The following antibodies were employed for visualization: rat anti-HA for
554 *Pf*Coronin-smHA (1:50; Sigma Cat. No. 11867423001), Sytox Far Red for DNA (ThermoFisher
555 Cat. No. S11380), rabbit anti-aldolase as a marker for parasite cytoplasm (1:2000; Abcam Cat.
556 No. ab207494), Streptavidin-488 for parasites containing internalized biotin-dextran (1:250;

557 Thermo Fisher Cat. No. S11223), and Alexa Fluor 405-conjugated NHS ester for protein density
558 (ThermoFisher Cat. No. A30000).

559 **Statistical analysis:** All experiments were performed with at least three biological replicates,
560 unless described otherwise. For volcano plots of proteins from *Pf*Coronin coIPs, *p*-values were
561 computed using unpaired t-tests. Protein quantifications (immunoblot) were compared using
562 paired t-tests. RSA assays were compared using unpaired *t*-tests with the Welch correction. Size
563 comparisons (e.g. parasite and invagination perimeters) were compared using unpaired t-tests.
564 Uptake of host cell contents (endocytosis assay) was compared using unpaired non-parametric
565 Mann-Whitney tests. The presence or absence of PPDC/invagination in WT and mutant parasites
566 was assessed using Fisher's exact test, specifically employing the Baptista-Pike method. Chi-
567 square analysis with the Baptista-Pike method was conducted to compare the presence or
568 absence of endocytosed fluorescein-dextran (visible fluorescence) between WT and mutant
569 parasites. All statistics were calculated using GraphPad Prism. No statistical methods were used
570 to predetermine sample sizes. Researchers were blinded for analysis of the endocytic assay
571 (uptake of host cell contents) and for all RSA assays.

572

573 **Acknowledgments**

574 Funding: NIH (5R01AI099105-07) to DFW and DLH.

575

576 **Author contributions**

577 Conceptualization: I.U., J.D.D., D.L.H., S.K.V., S.B., S.A., and D.F.W.; Methodology: I.U., M.A.F.,
578 A.Y.B., E.H., B.C.W., M.K., S.H.S., A.I.S., K.L.S., M.C.M., S.A.,; Data analyses: I.U., A.Y.B.,
579 B.C.W., M.K., M.C.M, S.H.S., S.A.,; Writing - original draft: I.U.; writing - review & editing: I.U.,
580 J.D.D., D.L.H., S.K.V., S.B., S.A., and D.F.W.; Funding acquisition: D.F.W., and D.L.H.,
581 Supervision: D.F.W.

582

583 # References

584 1. Bhatt, S. *et al.* The effect of malaria control on Plasmodium falciparum in Africa between
585 2000 and 2015. *Nature* **526**, 207–211 (2015).

586 2. van der Pluijm, R. W. *et al.* Triple artemisinin-based combination therapies versus
587 artemisinin-based combination therapies for uncomplicated Plasmodium falciparum
588 malaria: a multicentre, open-label, randomised clinical trial. *Lancet (London, England)*
589 **395**, 1345–1360 (2020).

590 3. Phyo, A. P. *et al.* Declining Efficacy of Artemisinin Combination Therapy Against P.
591 Falciparum Malaria on the Thai–Myanmar Border (2003–2013): The Role of Parasite
592 Genetic Factors. *Clin. Infect. Dis.* **63**, 784–791 (2016).

593 4. Ariey, F. *et al.* A molecular marker of artemisinin-resistant Plasmodium falciparum
594 malaria. *Nature* **505**, 50–55 (2014).

595 5. Birnbaum, J. *et al.* A Kelch13-defined endocytosis pathway mediates artemisinin
596 resistance in malaria parasites. *Science* **367**, 51–59 (2020).

597 6. Behrens, H. M., Schmidt, S. & Spielmann, T. The newly discovered role of endocytosis in
598 artemisinin resistance. *Med. Res. Rev.* **41**, 2998–3022 (2021).

599 7. Wang, J. *et al.* Haem-activated promiscuous targeting of artemisinin in Plasmodium
600 falciparum. *Nat. Commun.* **6**, 10111 (2015).

601 8. Demas, A. R. *et al.* Mutations in Plasmodium falciparum actin-binding protein coronin
602 confer reduced artemisinin susceptibility. *Proc. Natl. Acad. Sci. U. S. A.* **115**, 12799–
603 12804 (2018).

604 9. Sharma, A. I. *et al.* Genetic background and PfKelch13 affect artemisinin susceptibility of
605 PfCoronin mutants in Plasmodium falciparum. *PLoS Genet.* **16**, e1009266 (2020).

606 10. Tardieux, I. *et al.* A Plasmodium falciparum novel gene encoding a coronin-like protein
607 which associates with actin filaments. *FEBS Lett.* **441**, 251–6 (1998).

608 11. Eckert, C., Hammesfahr, B. & Kollmar, M. A holistic phylogeny of the coronin gene family
609 reveals an ancient origin of the tandem-coronin, defines a new subfamily, and predicts
610 protein function. *BMC Evol. Biol.* **11**, 268 (2011).

611 12. Stirnimann, C. U., Petsalaki, E., Russell, R. B. & Müller, C. W. WD40 proteins propel
612 cellular networks. *Trends Biochem. Sci.* **35**, 565–574 (2010).

613 13. Schapira, M., Tyers, M., Torrent, M. & Arrowsmith, C. H. WD40 repeat domain proteins: a
614 novel target class? *Nat. Rev. Drug Discov.* **16**, 773–786 (2017).

615 14. Chan, K. T., Creed, S. J. & Bear, J. E. Unraveling the enigma: progress towards
616 understanding the coronin family of actin regulators. *Trends Cell Biol.* **21**, 481–8 (2011).

617 15. Salamun, J., Kallio, J. P., Daher, W., Soldati-Favre, D. & Kursula, I. Structure of
618 Toxoplasma gondii coronin, an actin-binding protein that relocalizes to the posterior pole
619 of invasive parasites and contributes to invasion and egress. *FASEB J.* **28**, 4729–47
620 (2014).

621 16. Bane, K. S. *et al.* The Actin Filament-Binding Protein Coronin Regulates Motility in
622 Plasmodium Sporozoites. *PLoS Pathog.* **12**, e1005710 (2016).

623 17. Olshina, M. A. *et al.* Plasmodium falciparum coronin organizes arrays of parallel actin
624 filaments potentially guiding directional motility in invasive malaria parasites. *Malar. J.* **14**,
625 280 (2015).

626 18. Viswanathan, S. *et al.* High-performance probes for light and electron microscopy. *Nat.*
627 *Methods* **12**, 568–76 (2015).

628 19. Green, J. L. *et al.* Ubiquitin activation is essential for schizont maturation in Plasmodium
629 falciparum blood-stage development. *PLOS Pathog.* **16**, e1008640 (2020).

630 20. Liffner, B. & Absalon, S. Expansion Microscopy Reveals Plasmodium falciparum Blood-
631 Stage Parasites Undergo Anaphase with A Chromatin Bridge in the Absence of Mini-
632 Chromosome Maintenance Complex Binding Protein. *Microorganisms* **9**, (2021).

633 21. Liffner, B. *et al.* Atlas of Plasmodium falciparum intraerythrocytic development using
634 expansion microscopy. *bioRxiv Prepr. Serv. Biol.* (2023)
635 doi:10.1101/2023.03.22.533773.

636 22. Elliott, D. A. *et al.* Four distinct pathways of hemoglobin uptake in the malaria parasite
637 Plasmodium falciparum. *Proc. Natl. Acad. Sci. U. S. A.* **105**, 2463–8 (2008).

638 23. Smythe, W. A., Joiner, K. A. & Hoppe, H. C. Actin is required for endocytic trafficking in
639 the malaria parasite Plasmodium falciparum. *Cell. Microbiol.* **10**, 452–64 (2008).

640 24. Lazarus, M. D., Schneider, T. G. & Taraschi, T. F. A new model for hemoglobin ingestion
641 and transport by the human malaria parasite Plasmodium falciparum. *J. Cell Sci.* **121**,
642 1937–1949 (2008).

643 25. González-López, L. *et al.* Lys48 ubiquitination during the intraerythrocytic cycle of the
644 rodent malaria parasite, Plasmodium chabaudi. *PLoS One* **12**, e0176533 (2017).

645 26. Kudryashova, E., Kudryashov, D., Kramerova, I. & Spencer, M. J. Trim32 is a Ubiquitin
646 Ligase Mutated in Limb Girdle Muscular Dystrophy Type 2H that Binds to Skeletal Muscle
647 Myosin and Ubiquitinates Actin. *J. Mol. Biol.* **354**, 413–424 (2005).

648 27. Onishi, M., Pecani, K., Jones, T., Pringle, J. R. & Cross, F. R. F-actin homeostasis
649 through transcriptional regulation and proteasome-mediated proteolysis. *Proc. Natl. Acad.*
650 *Sci.* **115**, (2018).

651 28. No Title. doi:10.1128/mbio.03239-21.

652 29. Jonscher, E. *et al.* PfVPS45 Is Required for Host Cell Cytosol Uptake by Malaria Blood
653 Stage Parasites. *Cell Host Microbe* **25**, 166-173.e5 (2019).

654 30. Wagner, M. P. *et al.* Human peroxiredoxin 6 is essential for malaria parasites and
655 provides a host-based drug target. *Cell Rep.* **39**, 110923 (2022).

656 31. Taraschi, T. F. *et al.* Generation of an erythrocyte vesicle transport system by
657 Plasmodium falciparum malaria parasites. *Blood* **102**, 3420–3426 (2003).

658 32. Mukherjee, A. *et al.* A Phosphoinositide-Binding Protein Acts in the Trafficking Pathway of
659 Hemoglobin in the Malaria Parasite Plasmodium falciparum. *MBio* **13**, (2022).

660 33. Goode, B. L., Eskin, J. A. & Wendland, B. Actin and Endocytosis in Budding Yeast.
661 *Genetics* **199**, 315–358 (2015).

662 34. Doherty, G. J. & McMahon, H. T. Mechanisms of Endocytosis. *Annu. Rev. Biochem.* **78**,
663 857–902 (2009).

664 35. Sattler, J. M., Ganter, M., Hliscs, M., Matuschewski, K. & Schüler, H. Actin regulation in
665 the malaria parasite. *Eur. J. Cell Biol.* **90**, 966–971 (2011).

666 36. Olshina, M. A., Wong, W. & Baum, J. Holding back the microfilament--structural insights
667 into actin and the actin-monomer-binding proteins of apicomplexan parasites. *IUBMB Life*
668 **64**, 370–7 (2012).

669 37. Kumpula, E. P. & Kursula, I. Towards a molecular understanding of the apicomplexan
670 actin motor: on a road to novel targets for malaria remedies? *Acta Crystallogr. Sect. F,*
671 *Struct. Biol. Commun.* **71**, 500–13 (2015).

672 38. Stortz, J. F. *et al.* Formin-2 drives polymerisation of actin filaments enabling segregation
673 of apicoplasts and cytokinesis in Plasmodium falciparum. *Elife* **8**, (2019).

674 39. Henrici, R. C., van Schalkwyk, D. A. & Sutherland, C. J. Modification of pfap2µ and
675 pfubp1 Markedly Reduces Ring-Stage Susceptibility of Plasmodium falciparum to
676 Artemisinin In Vitro. *Antimicrob. Agents Chemother.* **64**, (2019).

677 40. Klonis, N. *et al.* Artemisinin activity against Plasmodium falciparum requires hemoglobin
678 uptake and digestion. *Proc. Natl. Acad. Sci.* **108**, 11405–11410 (2011).

679 41. Tsujita, K. *et al.* Proteome of acidic phospholipid-binding proteins: spatial and temporal
680 regulation of Coronin 1A by phosphoinositides. *J. Biol. Chem.* **285**, 6781–9 (2010).

681 42. Ehlgen, F., Pham, J. S., de Koning-Ward, T., Cowman, A. F. & Ralph, S. A. Investigation
682 of the Plasmodium falciparum food vacuole through inducible expression of the
683 chloroquine resistance transporter (PfCRT). *PLoS One* **7**, e38781 (2012).

684 43. Abu Bakar, N., Klonis, N., Hanssen, E., Chan, C. & Tilley, L. Digestive-vacuole genesis
685 and endocytic processes in the early intraerythrocytic stages of Plasmodium falciparum.
686 *J. Cell Sci.* **123**, 441–50 (2010).

687 44. Wendt, C., Rachid, R., de Souza, W. & Miranda, K. Electron tomography characterization
688 of hemoglobin uptake in Plasmodium chabaudi reveals a stage-dependent mechanism
689 for food vacuole morphogenesis. *J. Struct. Biol.* **194**, 171–179 (2016).

690 45. Diarra, H. *et al.* Molecular Investigation of Genetic Signatures of Selection in
691 </i>Plasmodium falciparum</i> Actin-Binding Protein
692 Coronin, Cysteine Desulfurase, and Plasmepsin 2 Gene in Mbita Field Isolates, Western
693 Kenya. *Open J. Genet.* **11**, 120–144 (2021).

694 46. Tumwebaze, P. K. *et al.* Decreased susceptibility of Plasmodium falciparum to both
695 dihydroartemisinin and lumefantrine in northern Uganda. *Nat. Commun.* **13**, 6353 (2022).

696 47. Ullah I, Sharma R, Mete A, Biagini GA, Wetzel DM, H. P. . The relative rate of kill of the
697 MMV Malaria Box compounds provide links to the mode of antimalarial action and
698 highlight scaffolds of medicinal chemistry interest. *J. Antimicrob. Chemother.* **75**, 362–370
699 (2019).

700 48. Ullah, I., Sharma, R., Biagini, G. A. & Horrocks, P. A validated bioluminescence-based
701 assay for the rapid determination of the initial rate of kill for discovery antimalarials. *J.*
702 *Antimicrob. Chemother.* **72**, 717–726 (2017).

703 49. Lambros, C. & Vanderberg, J. P. Synchronization of *Plasmodium falciparum* erythrocytic
704 stages in culture. *J. Parasitol.* **65**, 418–20 (1979).

705 50. Rudlaff, R. M., Kraemer, S., Streva, V. A. & Dvorin, J. D. An essential contractile ring
706 protein controls cell division in Plasmodium falciparum. *Nat. Commun.* **10**, 2181 (2019).

707 51. Bopp, S. *et al.* Potent acyl-CoA synthetase 10 inhibitors kill Plasmodium falciparum by
708 disrupting triglyceride formation. *Nat. Commun.* **14**, 1455 (2023).

709 52. Ariey, F. *et al.* A molecular marker of artemisinin-resistant Plasmodium falciparum
710 malaria. *Nature* **505**, 50–5 (2014).

711 53. Witkowski, B. *et al.* Novel phenotypic assays for the detection of artemisinin-resistant
712 Plasmodium falciparum malaria in Cambodia: in-vitro and ex-vivo drug-response studies.
713 *Lancet Infect. Dis.* **13**, 1043–1049 (2013).

714 54. Smilkstein, M., Sriwilaijaroen, N., Kelly, J. X., Wilairat, P. & Riscoe, M. Simple and
715 inexpensive fluorescence-based technique for high-throughput antimalarial drug
716 screening. *Antimicrob. Agents Chemother.* **48**, 1803–1806 (2004).

717 55. Johnson, J. D. *et al.* Assessment and Continued Validation of the Malaria SYBR Green I-
718 Based Fluorescence Assay for Use in Malaria Drug Screening. *Antimicrob. Agents*
719 *Chemother.* **51**, 1926–1933 (2007).

720 56. Ullah, I. *et al.* The relative rate of kill of the MMV Malaria Box compounds provides links
721 to the mode of antimalarial action and highlights scaffolds of medicinal chemistry interest.
722 *J. Antimicrob. Chemother.* **75**, (2020).

723 57. Rappsilber, J., Ishihama, Y. & Mann, M. Stop and Go Extraction Tips for Matrix-Assisted
724 Laser Desorption/Ionization, Nanoelectrospray, and LC/MS Sample Pretreatment in
725 Proteomics. *Anal. Chem.* **75**, 663–670 (2003).

726 58. Peng, J. & Gygi, S. P. Proteomics: the move to mixtures. *J. Mass Spectrom.* **36**, 1083–
727 1091 (2001).

728 59. Eng, J. K., McCormack, A. L. & Yates, J. R. An approach to correlate tandem mass
729 spectral data of peptides with amino acid sequences in a protein database. *J. Am. Soc.*
730 *Mass Spectrom.* **5**, 976–989 (1994).

731 60. Angrisano, F. *et al.* Spatial Localisation of Actin Filaments across Developmental Stages
732 of the Malaria Parasite. *PLoS One* **7**, e32188 (2012).

733 61. Vahokoski, J. *et al.* Structural differences explain diverse functions of Plasmodium actins.
734 *PLoS Pathog.* **10**, e1004091 (2014).

735

736

Figure 1

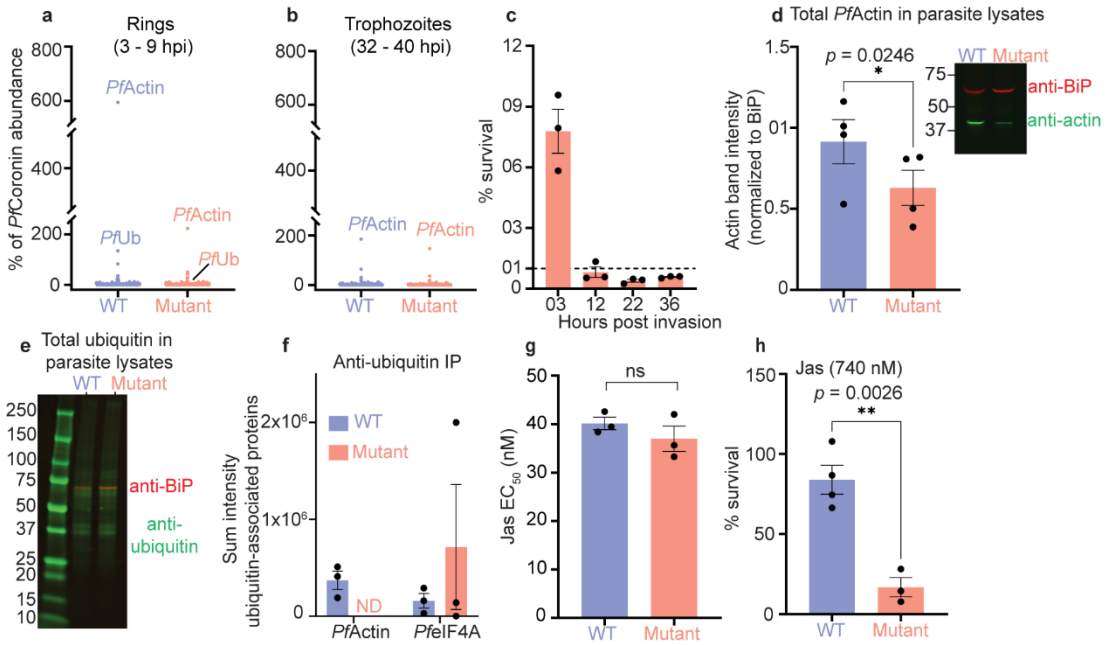

Fig. 1: Mutations in *Pfcoronin* alter *PfActin* homeostasis. (a) Immunoprecipitation of *Pf*Coronin-smHA and associated proteins in ring and (b) late trophozoite-stage parasites (n=4 rings; n = 6 trophozoites). (c) RSA survival (%) following 700 nM DHA pulse for 6-hour increments at various points in the intraerythrocytic developmental cycle. (d) Total *Pf*Actin levels in lysates from parasites expressing *Pf*Coronin$^{R100K/E107V}$-smHA (mutant) were compared by western blot to lysates from parasites expressing *Pf*Coronin^{WT}-smHA (representative blot shown). Blots were probed with anti-actin (mouse monoclonal; green) and anti-BiP (loading control; rabbit polyclonal, red) antibodies. Bar graph shows densitometric quantification of *Pf*Actin, normalized against *Pf*BiP. (e) Global ubiquitination in lysates from parasites expressing *Pf*Coronin^{WT}-smHA and *Pf*Coronin$^{R100K/E107V}$-smHA (mutant) were compared by western blot (representative blot shown). Blots were probed with an anti-ubiquitin (mouse mAb FK2, green) and anti-BiP (loading control; rabbit polyclonal red) antibodies. (f) Immunoprecipitation of anti-*Pf*Ub associated proteins. Complete results for all proteins are shown in Supplementary Data 5. Highly consistent proteins, i.e., those identified in all replicates of either *Pf*Coronin$^{R100K/E107V}$-smHA or *Pf*Coronin^{WT}-smHA, are shown in Supplementary Fig. 4c. (g) E_{50} values of JAS and (h) percent survival of parasites treated for 6 hrs., starting at 3 hpi, with 740 nM JAS.

756 **Figure 2**

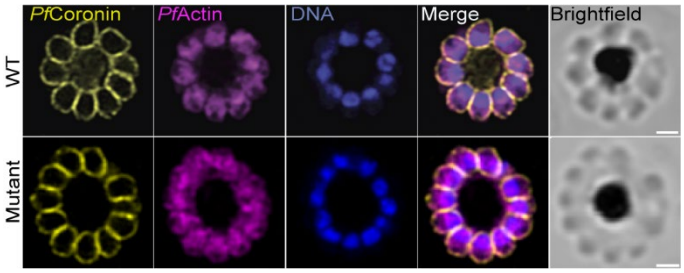

757

758 **Fig. 2: Immunofluorescent characterization of *Pf*Coronin and *Pf*Actin localization**. Super-
759 resolution fluorescence microscopy using Zeiss LSM980 with Airyscan2 shows localization of
760 *Pf*Coronin and *Pf*Actin in segmented schizonts. Scale bars = 2 µm.

761

762

763 **Figure 3**

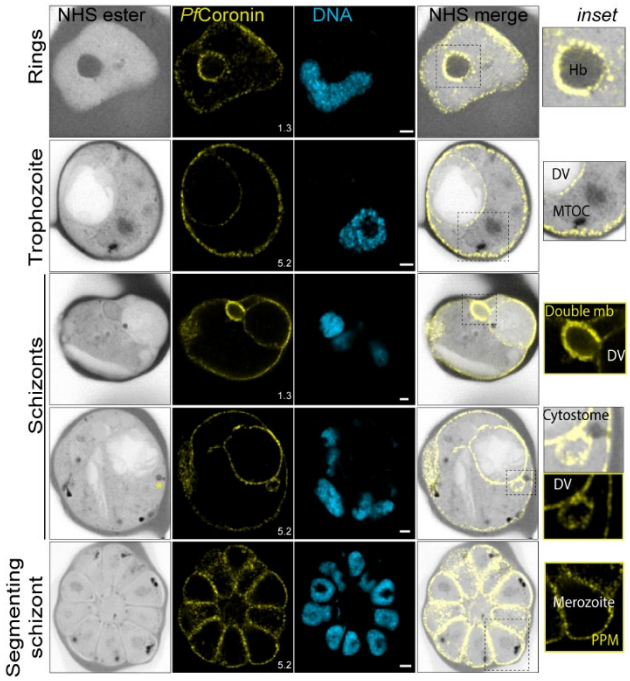

764

765 **Fig. 3: *Pf*Coronin marks ultrastructures in WT parasites throughout blood stage**
766 **development.** U-ExM shows *Pf*Coronin localization throughout the intraerythrocytic cycle in WT
767 parasites. Cytostome is marked with a yellow asterisk in the (NHS ester; schizonts). Alexa Fluor
768 405-conjugated NHS ester (protein density), HA (*Pf*Coronin, yellow), Sytox far red (DNA, Cyan).
769 Images are maximum-intensity projections; number on image = Z-axis thickness of projection in
770 µm. Scale bars = 2 µm.

771

Figure 4

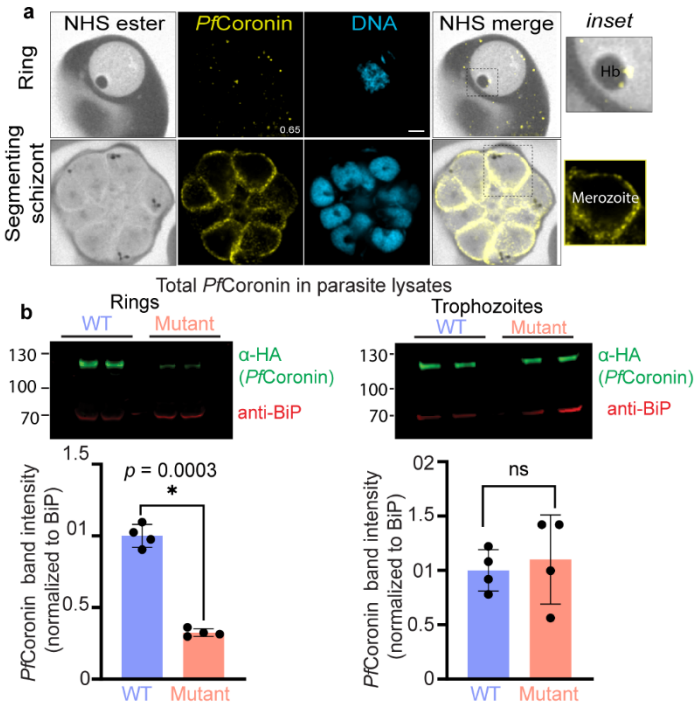

Fig. 4*: Pfcoronin* mutations impact localization and protein levels in rings. (a) U-ExM shows *Pf*Coronin$^{R100K/E107V}$-smHA (mutant) localization in rings and late schizont stage parasites. Alexa Fluor 405-conjugated NHS ester (protein density), HA (*Pf*Coronin, yellow), Sytox far red (DNA, Cyan). Images are maximum-intensity projections, number on image = Z-axis thickness of projection in µm. Scale bars = 2 µm. (b) Total *Pf*Coronin levels in lysates from parasites expressing *Pf*Coronin$^{R100K/E107V}$-smHA (mutant) were compared to lysates from parasites expressing *Pf*Coronin^{WT}-smHA via western blot (representative blot shown). Blots were probed with anti-HA (*Pf*Coronin; mouse monoclonal; green) and anti-BiP (loading control; rabbit polyclonal, red) antibodies. Bar graph shows densitometric quantification of *Pf*Coronin, normalized against *Pf*BiP.

786 **Figure 5**

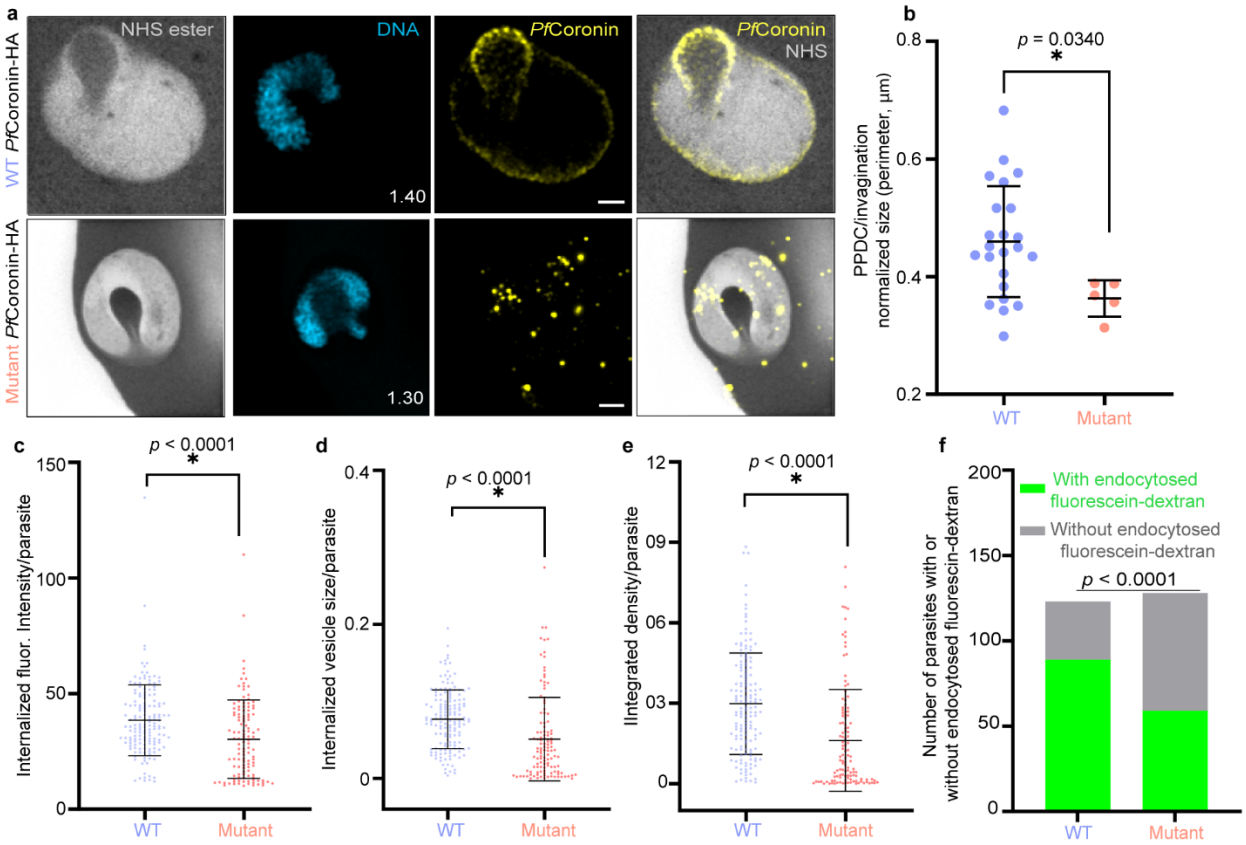

787

788 **Fig. 5: *Pfcoronin* mutations reduce invagination size and host cell content uptake.** (a)
789 Representative U-ExM images of *Pf*Coronin-labeled invaginations in *Pfcoronin*^{WT}*-smHA* and
790 *Pfcoronin*$^{R100K/E107V}$*-smHA* mutant parasites. Alexa Fluor 405-conjugated NHS ester (protein
791 density), HA (*Pf*Coronin, yellow), Sytox far red (DNA, cyan). Images are maximum-intensity
792 projections, with the number on the image indicating the Z-axis thickness of the projection in µm.
793 Scale bars = 2 µm. (b) Comparison of invagination perimeter in WT (n=23) vs. mutant (n=5)
794 parasites, normalized against parasite perimeter. See Supplementary Fig. 11d for parasite size
795 measurements. *p*-value (unpaired t-test) and % reduction of the mean are indicated. (c)
796 Comparison of internalized fluorescein-dextran in WT vs. mutant (R100K/E107V) *Pfcoronin*
797 parasites by (c) internalized fluorescence intensity (arbitrary fluorescence units), (d) vesicle size
798 (area), and (e) integrated density (vesicle size + intensity). WT *Pfcoronin*; n = 155, mutant
799 *Pfcoronin*; n = 120. Each data point represents fluorescein-dextran uptake by a single parasite.
800 *p*-values (unpaired, nonparametric Mann-Whitney test) and % reduction of the mean are
801 indicated. These data were pooled from the individual biological replicates shown in
802 Supplementary Fig. 14. (f) Comparison of *Pfcoronin*^{WT} and *Pfcoronin*$^{R100K/E107V}$ (mutant) parasites
803 in the early ring stage. Parasites were assessed for the presence or absence of endocytosed
804 fluorescein-dextran (visible fluorescence). WT and mutant parasites were compared using Chi-
805 square analysis (Baptista-Pike method); n = number of parasites analyzed (WT = 123, mutant =
806 128), pooled from 3 independent biological replicates, as shown in Supplementary Fig. 16.

807

808 **Figure 6**

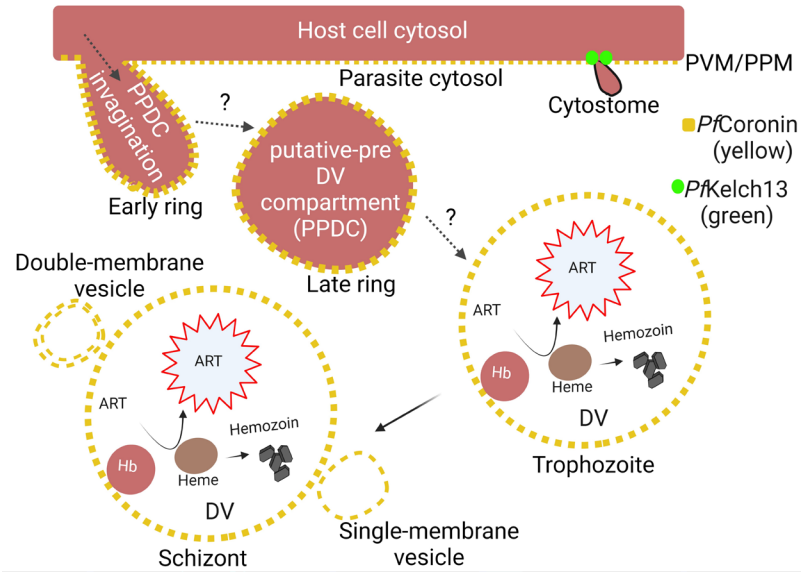

809

810 **Fig. 6: Working model for DV development, endocytosis, and *Pfcoronin*-mediated ART**
811 **resistance.** Diagram of infected RBC demonstrating hemoglobin uptake and associated
812 structures throughout parasite development, as well as subsequent hemoglobin digestion and
813 ART activation.

814

815

816

817

818 **Supplementary Figure 1**

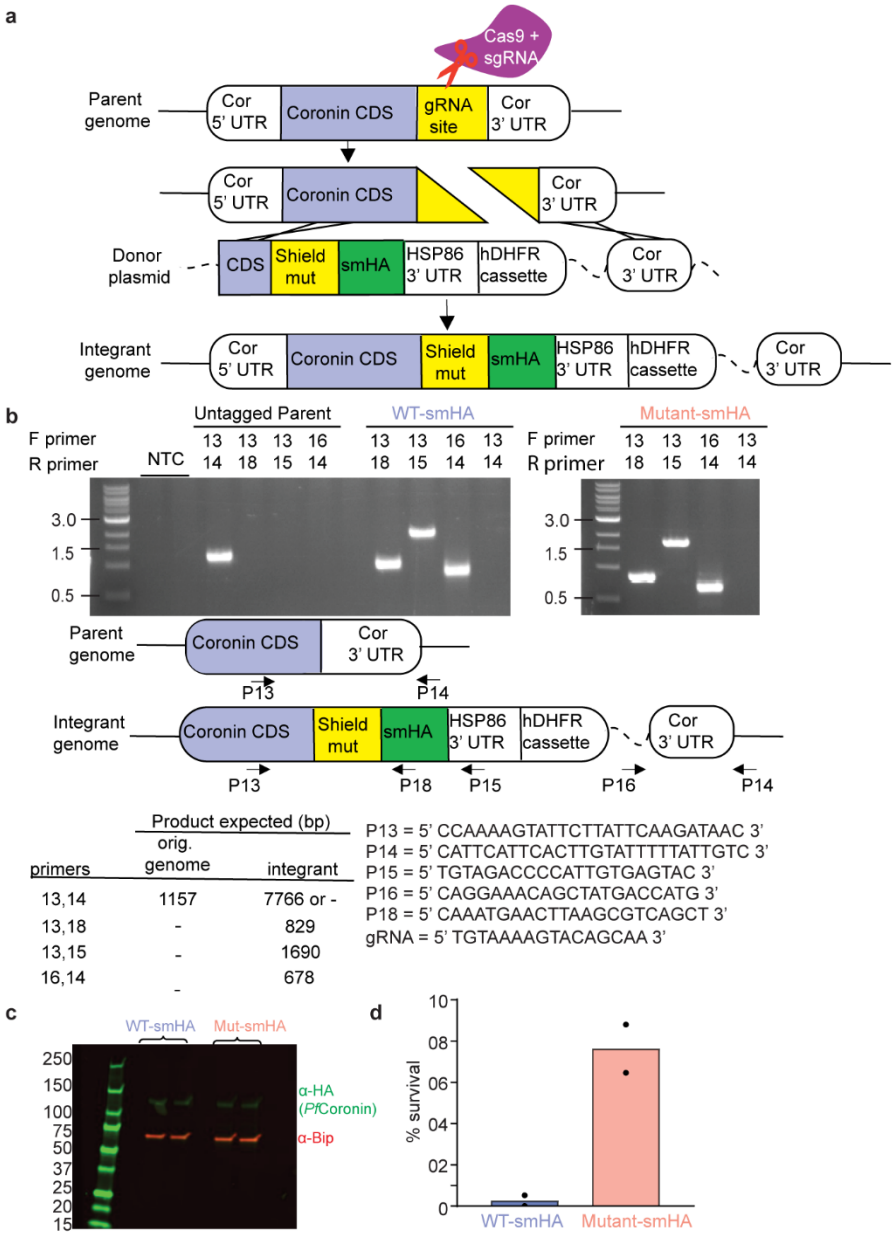

819

820

821 **Supplementary Fig. 1:** Generation of spaghetti monster HA tag (smHA)-tagged *Pfcoronin*^{WT}-
822 *smHA* and *Pfcoronin*$^{R100K/E107V}$*-smHA* transgenic lines. (a) Schematic for C-terminal endogenous
823 tagging of WT (*Pfcoronin*^{WT}) and mutant (*Pfcoronin*$^{R100K/E107V}$) parasites with smHA. Cas9 created
824 a double-stranded break near the C-terminus of the *Pfcoronin* locus in either the *Pfcoronin*^{WT} or
825 the *Pfcoronin*$^{R100K/E107V}$ parent strain. This break was subsequently repaired via double
826 crossover/homologous recombination between the *Pfcoronin* coding sequence (CDS; upstream
827 of the break), the *Pfcoronin* 3' UTR, and matching sequences on the donor vector. This resulted
828 in the integration of the entire donor vector, including an smHA tag appended to the C-terminus

829 of *Pfcoronin.* (b) PCR confirmation of smHA tagging in *Pfcoronin*^{WT}*-smHA* and
830 *Pfcoronin*$^{R100K/E107V}$*-smHA* lines. Expected sizes from PCRs using genomic DNA templates from
831 untagged (parental/ "orig. genome") *Pfcoronin* and *Pfcoronin-smHA* ("integrant") lines are detailed
832 in the associated table. Primers used for the PCRs are shown and their binding positions are
833 annotated in the schematic of the parasite genome. The gRNA sequence used is also shown. (c)
834 Confirmation of smHA-tagged *Pfcoronin*^{WT}*-smHA* and *Pfcoronin*$^{R100K/E107V}$*-smHA* lines via western
835 blotting using anti-HA tag (mouse mAb 2-2.2.14; green) and anti-BiP (loading control; rabbit
836 polyclonal red) antibodies; samples were generated from late-stage parasites. Two biological
837 replicates are shown for each strain. (d) Tightly synchronized 3-hour-old ring-stage *Pfcoronin*^{WT}-
838 *smHA* and *Pfcoronin*$^{R100K/E107V}$*-smHA* parasites were pulsed with 700 nM DHA for 6-hours, and
839 survival was assessed 66 hours later. As expected, substantial survival (i.e., artemisinin
840 resistance) was observed in the *Pfcoronin*$^{R100K/E107V}$*-smHA* line. Generally, the minimum survival
841 threshold for ART resistance is 1%. Means from two independent biological replicates are shown.

842

843

844 **Supplementary Figure 2**

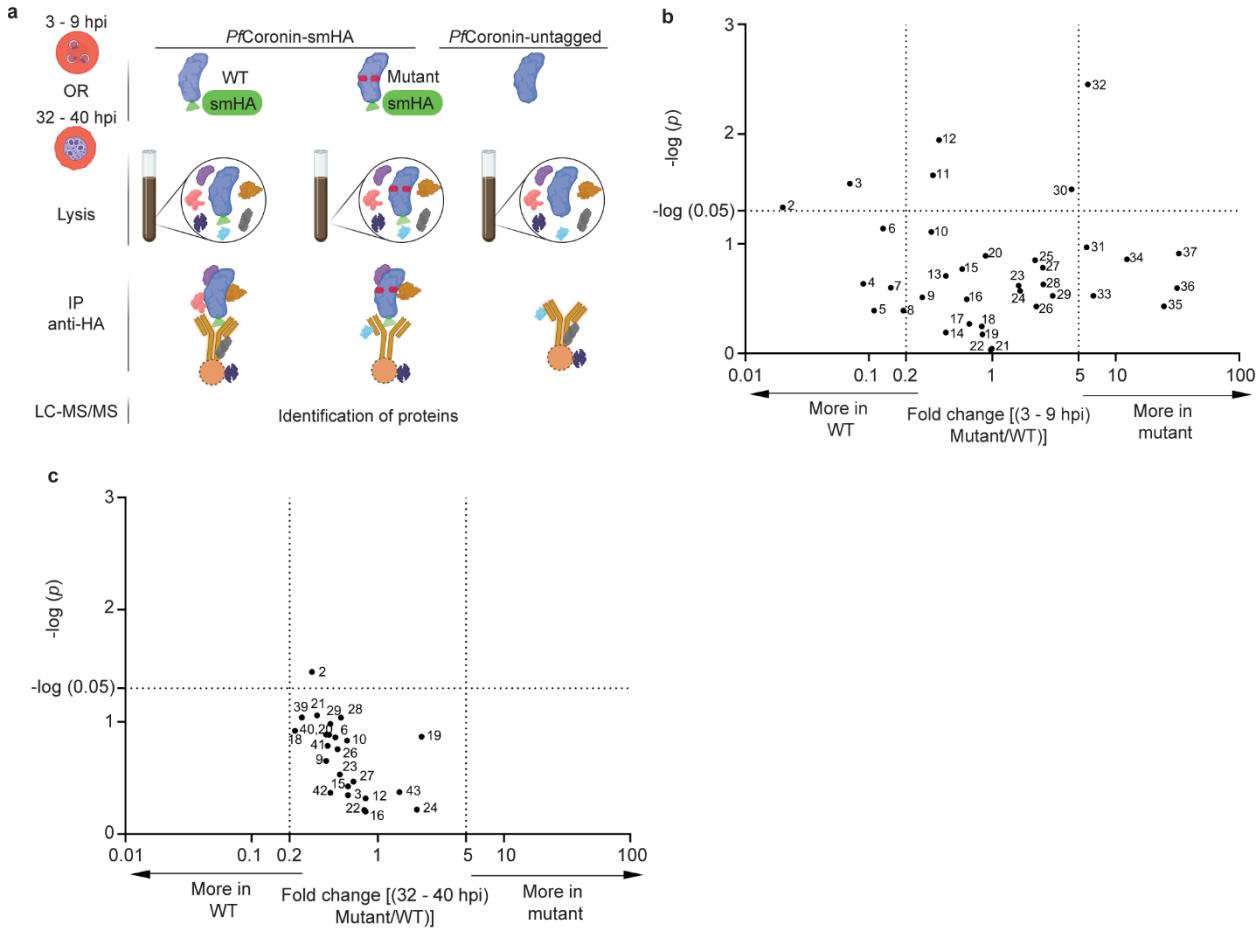

845

846 **Supplementary Fig. 2:** (a) Immunoprecipitation of *Pf*Coronin-smHA and associated proteins from
847 young ring-stage (3-9 h) and late-stage (32-40 h) parasites using anti-HA antibodies. Co-purified
848 proteins were identified by LC-MS/MS, with an untagged *Pfcoronin*^{WT} control used to filter
849 nonspecific interactions. hpi = hours post invasion. (b-c) A volcano plot of hit interaction partners
850 shows changes between *Pf*Coronin^{WT}-smHA and *Pf*Coronin$^{R100K/E107V}$-smHA in (a) rings, (b)
851 trophozoites. The x-axis shows the fold change between *Pf*Coronin^{WT}-smHA and
852 *Pf*Coronin$^{R100K/E107V}$-smHA bait proteins. The Y axis shows the statistical significance of the
853 change between *Pf*Coronin^{WT} and *Pf*Coronin$^{R100K/E107V}$ (unpaired t-test). The 37 hit proteins (for
854 rings in a) and 24 hit proteins (for trophozoites in b) plotted on the volcano plot were found in all
855 bioreps (either *Pf*Coronin^{WT}-smHA or *Pf*Coronin$^{R100K/E107V}$-smHA) and have at least 5% of the
856 *Pf*Coronin protein abundance. In rings (a) two proteins (#1, *Pf*3D7_0517700, eukaryotic
857 translation initiation factor 3 subunit B; and #38, *Pf*3D7_1424400, 60S ribosomal protein L7-3,
858 putative) fulfilled these criteria but could not be displayed because they were detected only in
859 *Pf*Coronin^{WT}-smHA (*Pf*3D7_0517700) or only in *Pf*Coronin$^{R100K/E107V}$-smHA pulldowns
860 (*PF*3D7_1424400), so a log fold change could not be computed. A full list of hit proteins can be
861 found in Supplementary Data 3 (for rings) and Supplementary Data 4 (for trophozoites). Proteins
862 of interest are defined as either those with $p < 0.05$ (above the dotted line on the y-axis), or a 5-
863 fold or greater change between *Pf*Coronin^{WT}-smHA and *Pf*Coronin$^{R100K/E107V}$-smHA parasites (to

the left (0.2) or right (5) of the vertical dotted lines on the x-axis). The proteins are numbered and are detailed in Supplementary Data 3 (for rings) and Supplementary Data 4 (for trophozoites). Each data point represents two or three independent biological replicates for rings and trophozoites, respectively.

869 **Supplementary Figure 3**

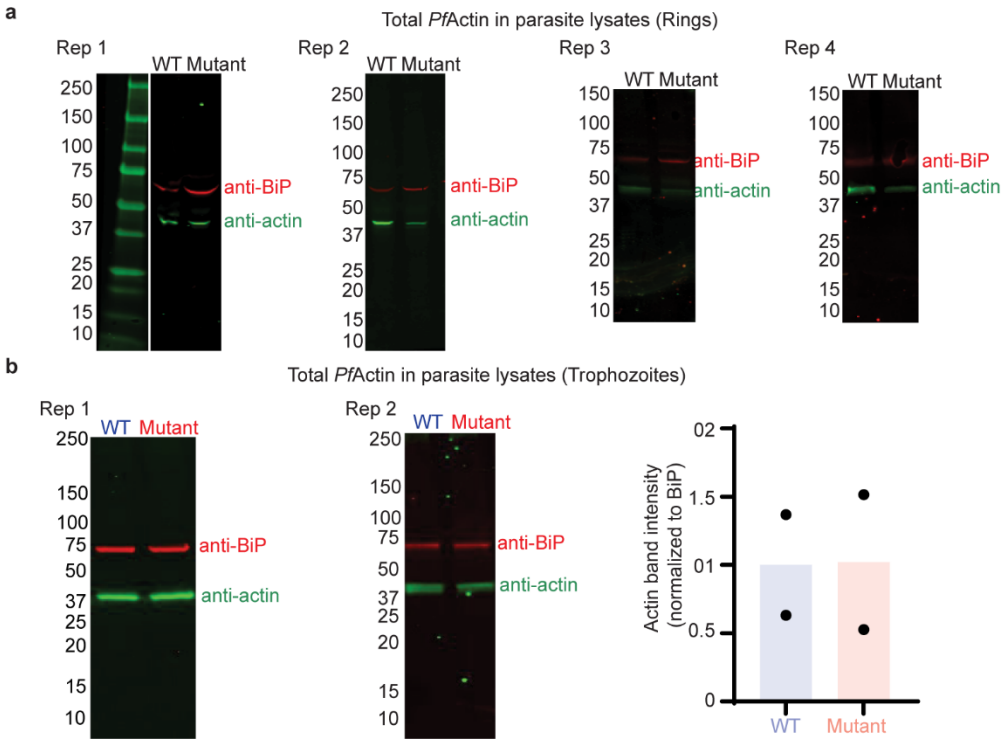

870

871 **Supplementary Fig. 3:** (a) Total *Pf*Actin is reduced in parasites expressing *Pf*Coronin$^{R100K/E107V}$-
872 smHA (mutant), compared to *Pf*Coronin^{WT}-smHA (WT). Lysates from parasites expressing
873 *Pf*Coronin$^{R100K/E107V}$-smHA were compared by western blot to lysates from parasites expressing
874 *Pf*Coronin^{WT}-smHA. Blots were probed with anti-actin (mouse monoclonal; green) and anti-BiP
875 (loading control; rabbit polyclonal, red) antibodies. All western blots quantified in Fig. 1d (biological
876 replicates 1-4) are shown. (b) Total *Pf*Actin in parasites expressing *Pf*Coronin$^{R100K/E107V}$-smHA
877 (mutant), compared to *Pf*Coronin^{WT}-smHA (WT) is not changed in late trophozoite stage parasites.
878 Blots were probed with anti-actin (mouse monoclonal; green) and anti-BiP (loading control; rabbit
879 polyclonal, red) antibodies. Quantification was based on the two independent biological replicates
880 shown.

881

882 **Supplementary Figure 4**

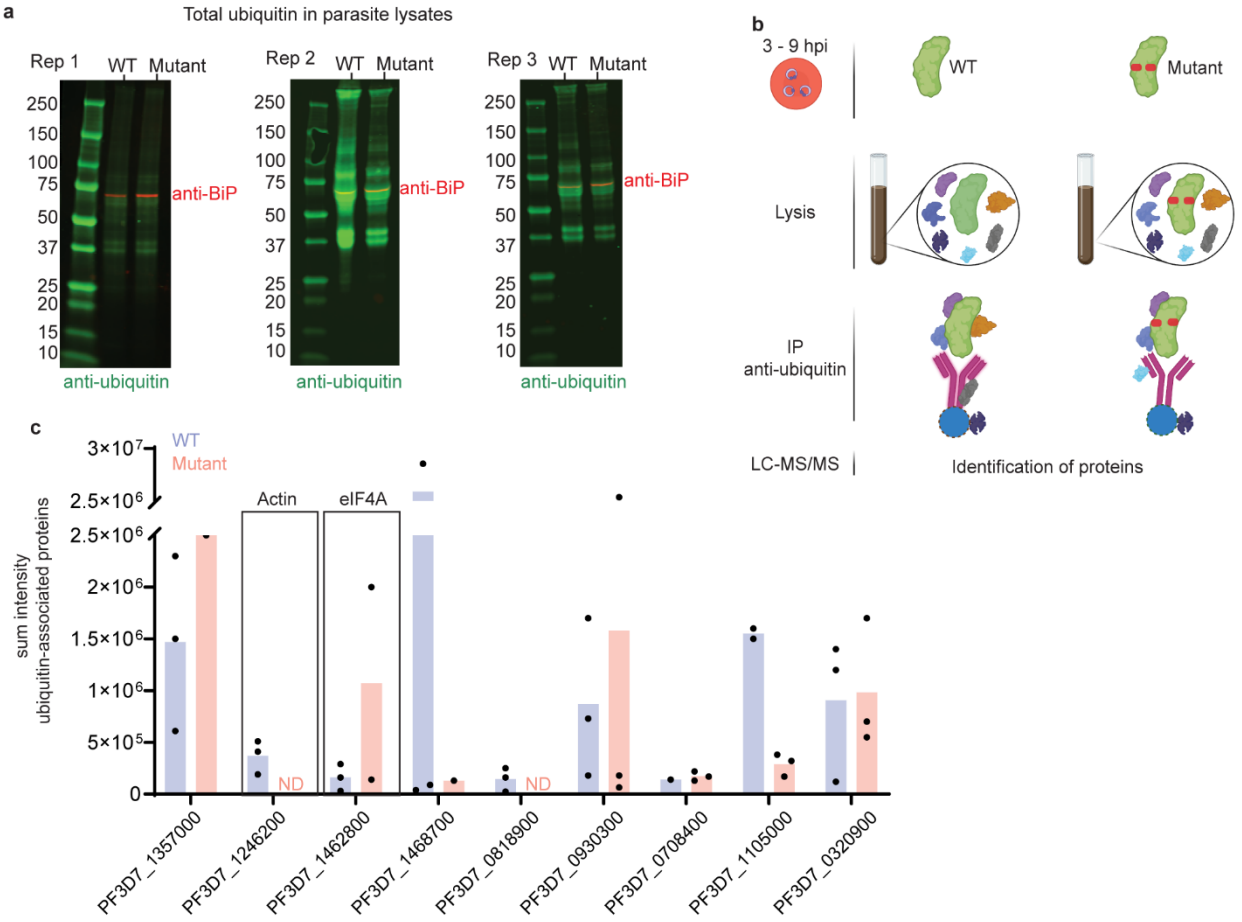

883

884 **Supplementary Fig. 4:** (a) No gross differences in global ubiquitination were observed in
885 parasites expressing *Pf*Coronin$^{R100K/E107V}$-smHA (mutant), compared to *Pf*Coronin^{WT}-smHA (WT).
886 Lysates from parasites expressing *Pf*Coronin^{WT}-smHA and *Pf*Coronin$^{R100K/E107V}$-smHA were
887 compared by western blot. Blots were probed with anti-ubiquitin (mouse mAb FK2, green) and
888 anti-BiP (loading control; rabbit polyclonal red) antibodies. Three independent biological
889 replicates are shown. (b) Schematic showing immunoprecipitation of ubiquitin and associated
890 proteins from young ring-stage parasites (3-9 h). (c) Comparison of *Pf*Ub-associated hit protein
891 abundances from parasites expressing *Pf*Coronin^{WT}-smHA vs *Pf*Coronin$^{R100K/E107V}$-smHA.
892 Following anti-ubiquitin IP, co-purified proteins were identified and quantified by LC-MS/MS.
893 Proteins shown were identified in all replicates of either *Pf*Coronin^{WT}-smHA or *Pf*Coronin$^{R100K/E107V}$-
894 smHA IPs. *Pf*Actin and *Pf*eIF4A, the only two proteins that were also identified as *Pf*Coronin
895 interaction partners (anti-HA IPs), are highlighted with boxes. Data shown are average
896 measurements from three independent biological replicates. Complete results are shown in
897 Supplementary Data 5.

898

899

900

Supplementary Figure 5

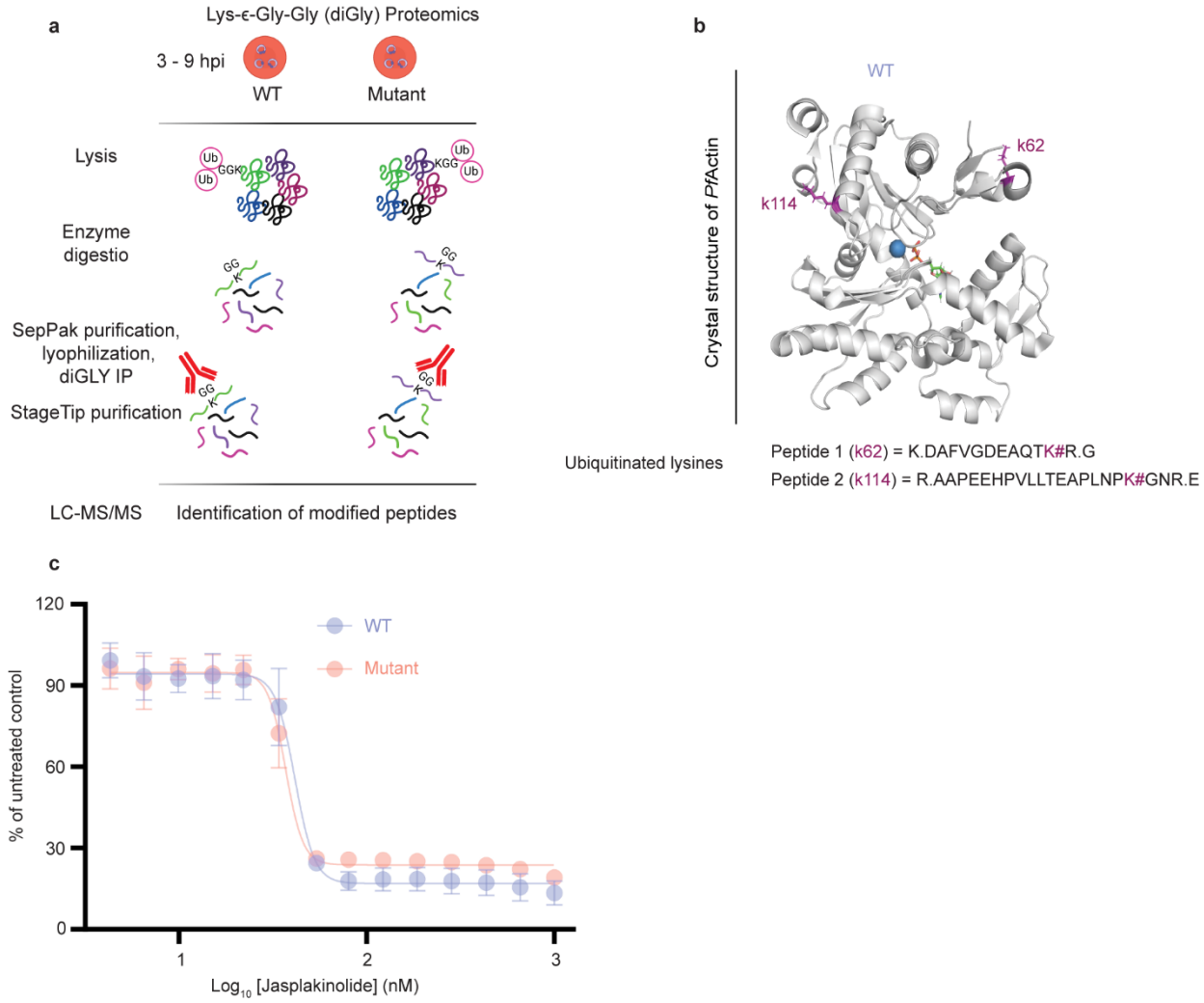

Supplementary Fig. 5: Lys-ϵ-Gly-Gly (diGly) proteomics to identify proteins that are ubiquitinated at specific sites. (a) Young ring-stage *Pfcoronin*^{WT} and *Pfcoronin*$^{R100K/E107V}$ parasites (3-9 h) were lysed, normalized by protein concentration, and subjected to trypsin digestion. Peptides were enriched with an anti-diGly antibody, and peptides were identified by LC-MS/MS. (b) Crystal structure of *Pf*Actin[61] . The ubiquitination sites identified are labelled and the individual peptides identified are detailed in Supplementary Data 6. (c) A standard 72-h assay shows no difference between WT (EC_{50} = 40.1 ± 1.3 nM) and mutant (EC_{50} = 37 ± 2.6 nM). Data points shown are average measurements from three independent biological replicates.

915 ## Supplementary Figure 6

916 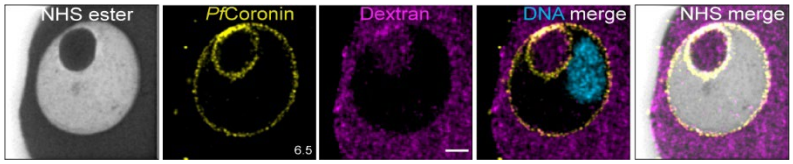

917 **Supplementary Fig. 6:** A representative image from ultrastructure expansion microscopy (U-
918 ExM), showing *Pf*Coronin-labeled intracellular putative pre-DV compartment (PPDC) housing
919 host cell contents, as indicated by dextran staining. This pattern is consistent across all analyzed
920 ring-stage PPDCs in *Pfcoronin*^{WT} parasites. Alexa Fluor 405-conjugated NHS ester (protein
921 density), HA (*Pf*Coronin, yellow), Streptavidin 488 (dextran, magenta), Sytox Far Red (DNA,
922 Cyan). The images are maximum-intensity projections, with the number indicating the Z-axis
923 thickness in µm. Scale bars: 2 µm

924

925 ## Supplementary Figure 7

926 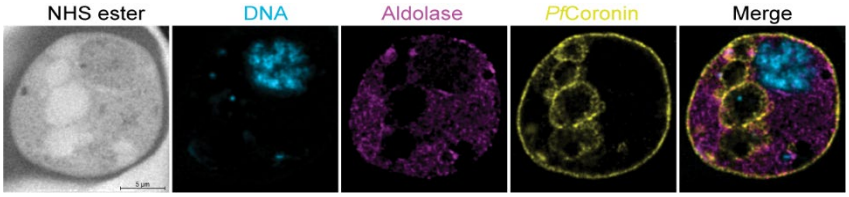

927 **Supplementary Fig. 7:** A representative image from ultrastructure expansion microscopy,
928 showing *Pf*Coronin-labeled intracellular chains of small and large vacuoles in a trophozoite. Alexa
929 Fluor 405-conjugated NHS ester (protein density), Sytox Far Red (DNA, cyan), Aldolase 555 for
930 parasite cytoplasm (magenta), HA (*Pf*Coronin, yellow). The images are maximum-intensity
931 projections.

932

933 **Supplementary Figure 8**

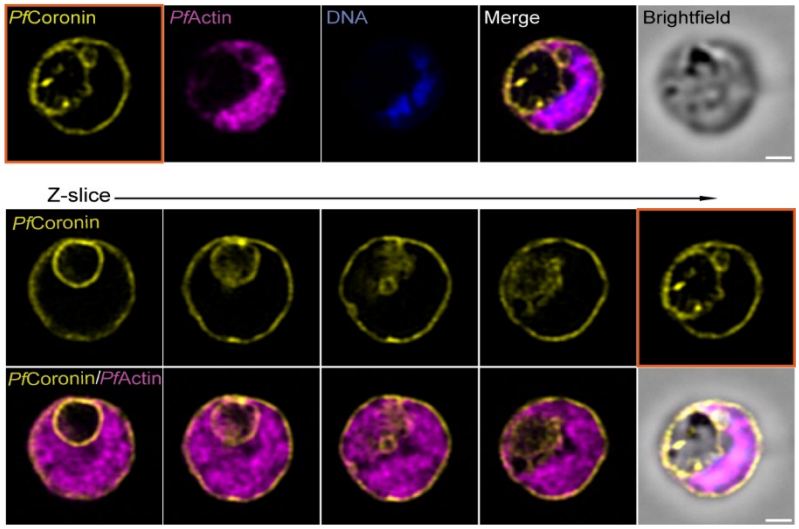

934

935 **Supplementary Fig. 8:** Super-resolution fluorescence microscopy using Zeiss LSM980 with
936 Airyscan2 shows localization of *Pf*Coronin and *Pf*Actin early schizont stage parasites. Scale bar
937 = 2 µm.

938

939 **Supplementary Figure 9**

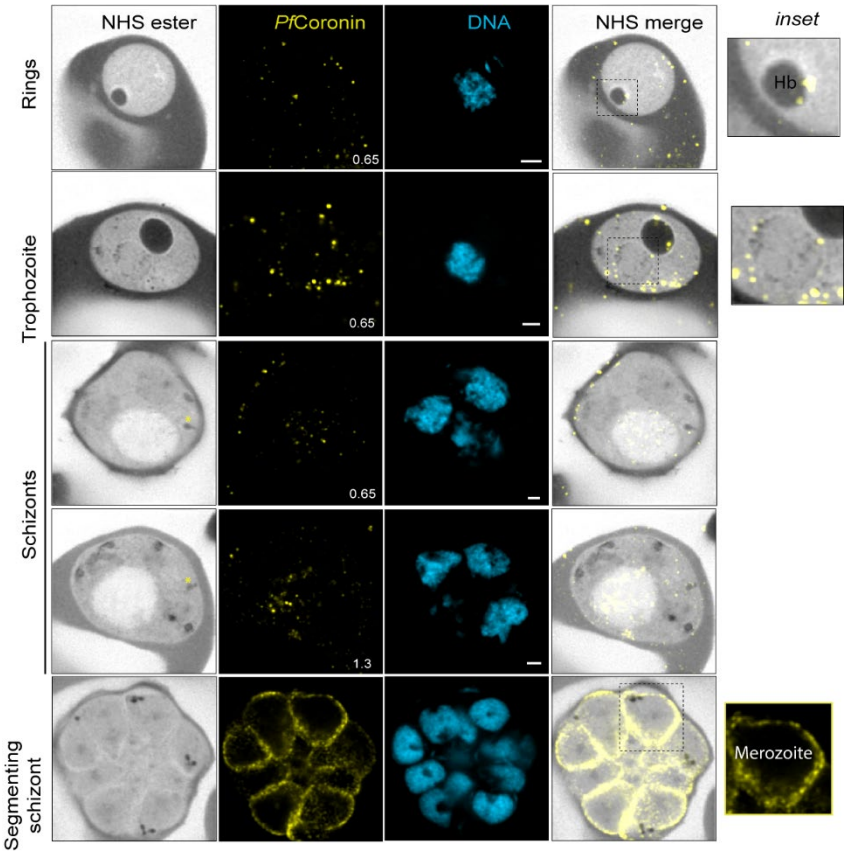

940

941

942 **Supplementary Fig. 9:** U-ExM shows *Pf*Coronin localization throughout the blood-stage cycle in
943 *Pfcoronin*$^{R100K/E107V}$*-smHA* mutant parasites. Cytostomes are marked with a yellow asterisk in the
944 first (NHS ester) panel of each row. Alexa Fluor 405-conjugated NHS ester (protein density), HA
945 (*Pf*Coronin, yellow), Sytox Far Red (DNA, cyan). Images are maximum-intensity projections,
946 number on image = Z-axis thickness of projection in µm. Scale bars = 2 µm.

947

948

949 **Supplementary Figure 10**

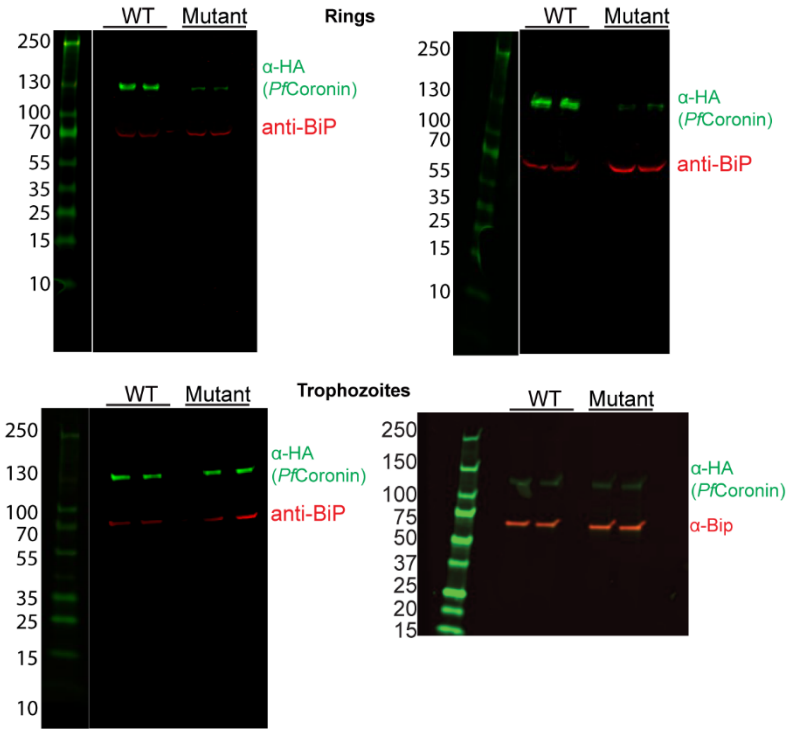

950

951 **Supplementary Fig. 10**: Total *Pf*Coronin levels in lysates from parasites expressing
952 *Pf*Coronin$^{R00K/E107V}$-smHA (mutant) were compared by western blot to lysates from parasites
953 expressing *Pf*Coronin^{WT}-smHA. Blots were probed with anti-HA (mouse monoclonal; green) and
954 anti-BiP (loading control; rabbit polyclonal, red) antibodies. All western blots quantified in Fig. 4b
955 are shown.

956

957 **Supplementary Figure 11**

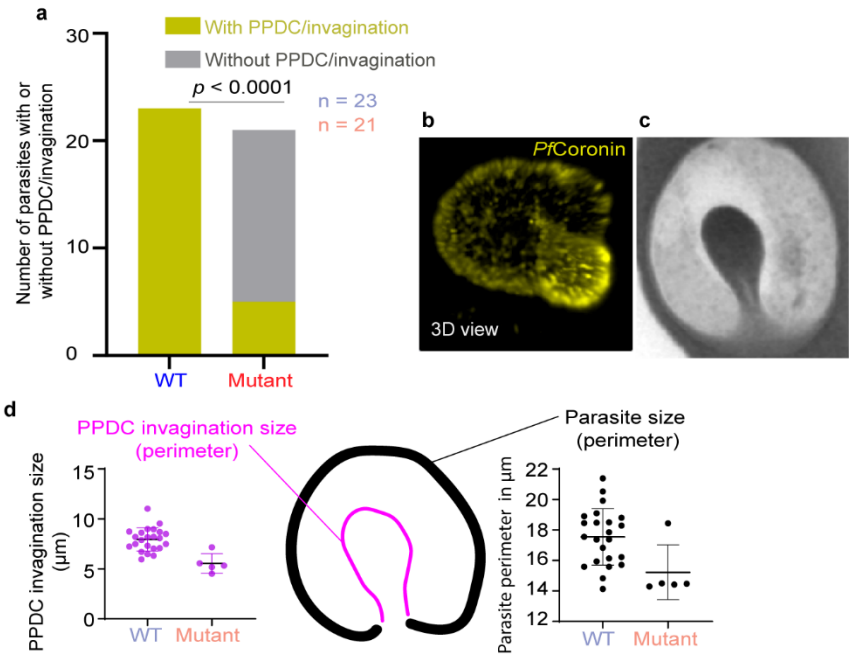

958

959

960 **Supplementary Fig. 11:** (a) *Pfcoronin*^{WT}*-smHA* and *Pfcoronin*$^{R100K/E107V}$*-smHA* (mutant) parasites
961 at the early ring stage (< 9hpi), compared for the presence of a PPDC/invagination, analyzed
962 using Fisher's exact test (Baptista-Pike method). (b) 3D view of *Pf*Coronin staining (anti-HA) of a
963 ring-stage parasite, displaying the parasite body and PPDC invagination. (c) NHS-ester staining
964 shows the parasite body and invagination. (d) Cartoon showing the measurement of
965 PPDC/invagination (left graph in magenta showing individual measurements) and parasite size
966 (right graph showing individual measurements of parasite size). PPDC/invagination sizes (left
967 graph) for both WT and mutant parasites were normalized against parasite size (right graph), and
968 the resulting data are presented in Fig 5b.

969

970 # Supplementary Figure 12

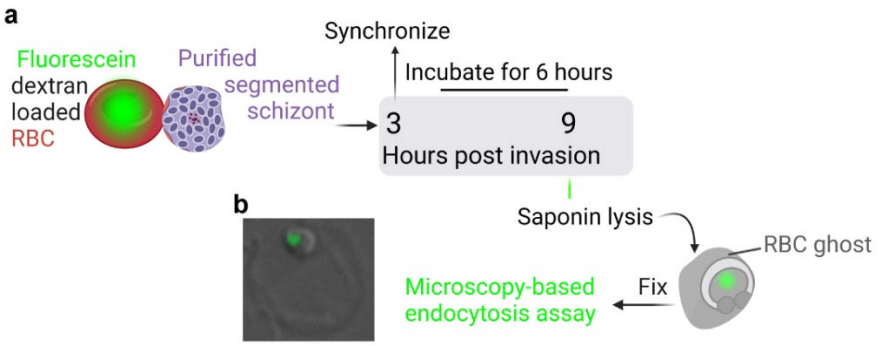

971

972 **Supplementary Fig. 12:** (**a**) Diagram of sample preparation for endocytosis. RBCs were lysed in
973 a hypotonic solution containing fluorescein-dextran. After re-sealing the RBCs (trapping the
974 fluorescein dextran within), schizonts were added and allowed to re-invade for 3 hours. As the
975 parasites (rings) grew within the fluorescein-dextran-containing RBCs, fluorescein-dextran was
976 endocytosed and accumulated in the DV and other compartments. The parasites were then
977 synchronized to remove any remaining schizonts and allowed to grow for a further 6 hrs, closely
978 mimicking the RSA setup. RBC cell contents were removed by saponin lysis and parasites were
979 fixed for microscopy. (**b**) DIC and AF488 channel images were captured using a 100X oil
980 immersion objective on a Zeiss Axio Observer. Representative image is shown. Images were
981 blinded prior to analysis. Analysis was carried out for regions of interest (ROIs) where an RBC
982 ghost could be visualized around a green channel signal in the merged image. Vesicle size (area),
983 internalized fluorescence intensity (mean gray value), and integrated density (over the entire
984 vesicle) of green-channel fluorescence signal was assessed.

985

986

987 **Supplementary Figure 13**

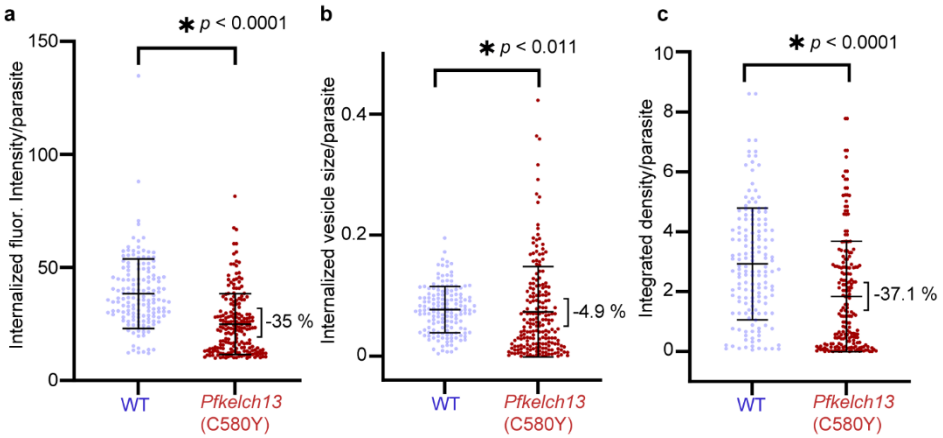

988

989 **Supplementary Fig. 13:** Comparison of internalized fluorescein-dextran in WT vs. *Pfkelch13*
990 (C580Y) parasites by (a) internalized fluorescence intensity (arbitrary fluorescence units), (b)
991 vesicle size, and (c) integrated density (vesicle size x intensity). WT *Pfcoronin* n = 155; *Pfkelch13*
992 (C580Y) n = 199. Each data point represents fluorescein-dextran uptake by a single parasite. *p*-
993 values (unpaired, nonparametric Mann-Whitney test) and % reduction of the mean are indicated.
994 These data were pooled from the individual biological replicates shown in Supplementary Fig. 15.

995

Supplementary Figure 14

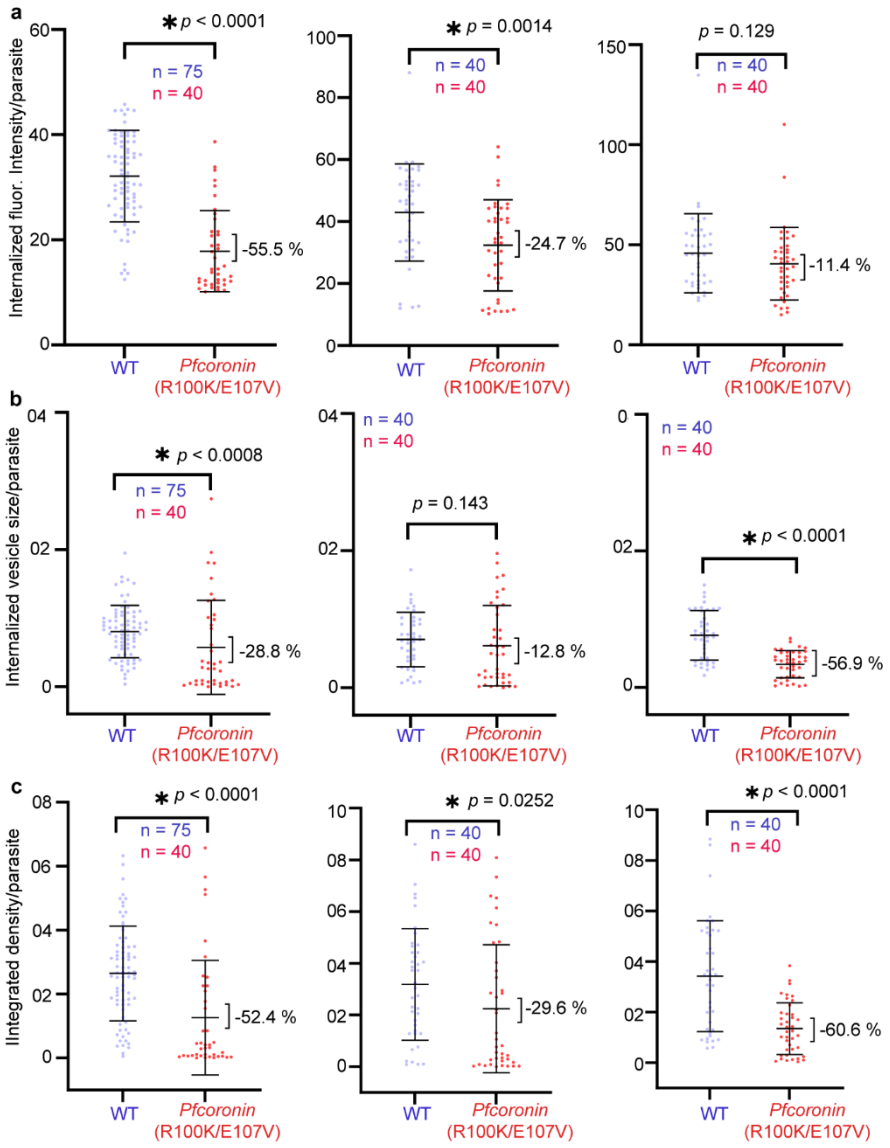

Supplementary Fig. 14: Individual biological replicates of internalized fluorescein-dextran in WT vs. *Pfcoronin* (R100K/E107V) mutant ring-stage parasites (3-9 hours post-invasion) quantified and pooled in Fig. 5. (a) Internalized fluorescence intensity (arbitrary fluorescence units), (b) vesicle size, and (c) integrated density (vesicle size x intensity). Each data point represents fluorescein-dextran uptake by a single parasite. *p*-values (calculated using an unpaired, nonparametric Mann-Whitney test) and % reduction of the mean are indicated. Number of cells = n. Bars show SD.

1006 **Supplementary Figure 15**

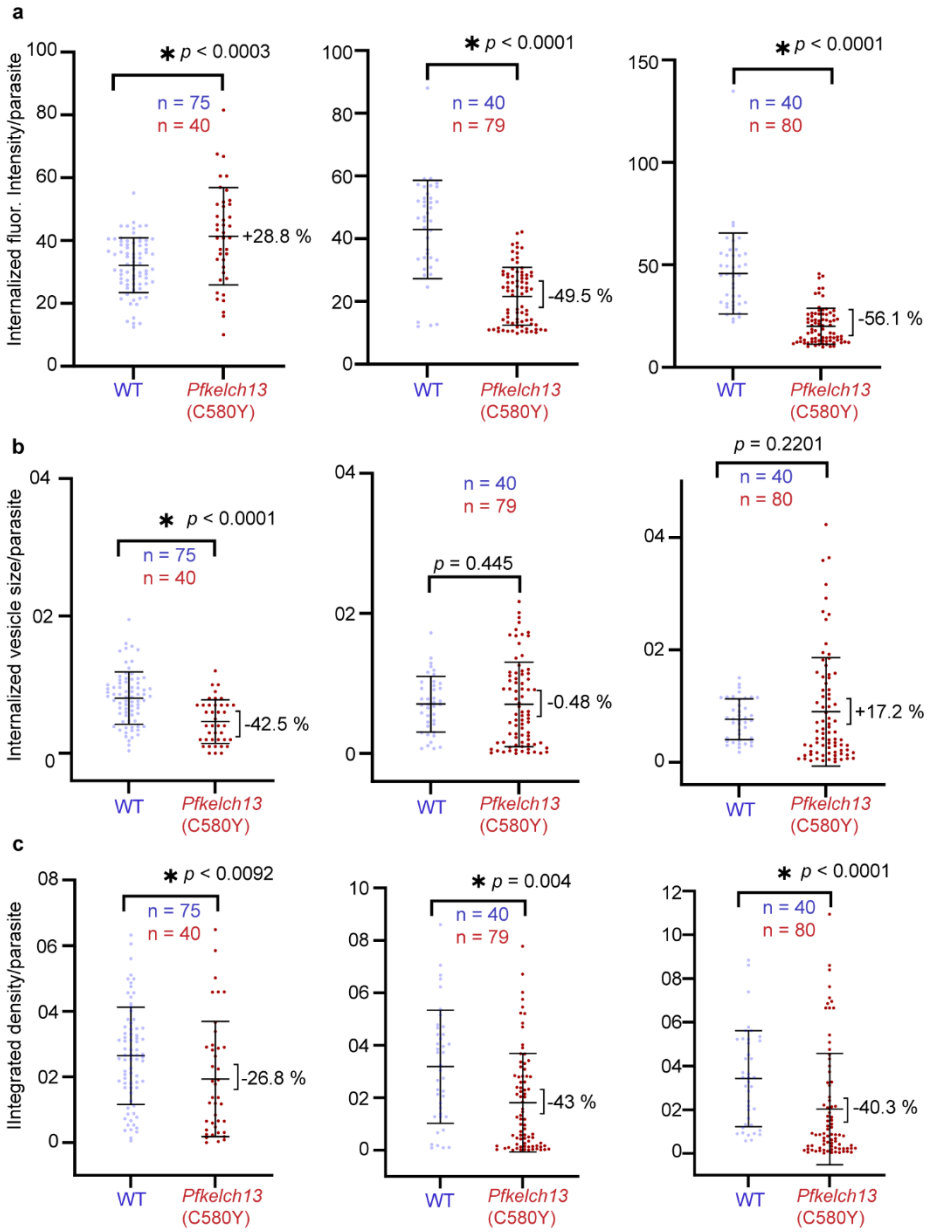

1007

1008 **Supplementary Fig. 15:** Individual biological replicates of internalized fluorescein-dextran in WT
1009 vs. 3D7 *Pfkelch13* (C580Y) mutant ring-stage parasites (3-9 hours post-invasion) quantified and
1010 pooled in Supplementary Fig. 13. (a) Internalized fluorescence intensity (arbitrary fluorescence
1011 units), (b) vesicle size, and (c) integrated density (vesicle size x intensity). Each data point
1012 represents fluorescein-dextran uptake by a single parasite. *p*-values (calculated using an
1013 unpaired, nonparametric Mann-Whitney test) and % reduction (-) or increase (+) of the mean are
1014 indicated. Number of cells = n. Bars show SD.

1015

1016 **Supplementary Figure 16**

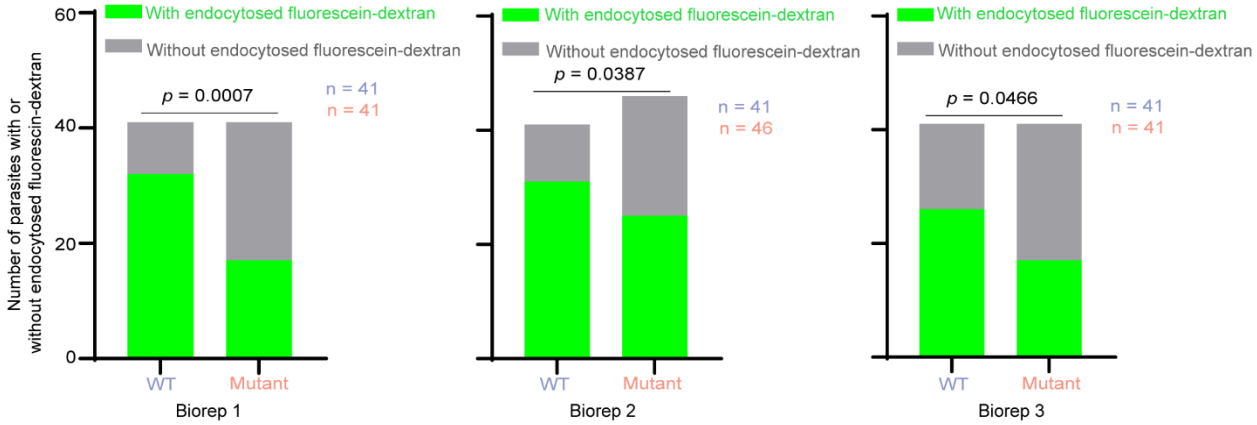

1017

1018 **Supplementary Fig. 16**: Compares WT and mutant parasites in the early ring stage (3-9 hpi).
1019 Parasites were assessed for the presence/absence of endocytosed fluorescein-dextran (visible
1020 fluorescence). Chi-square analysis (Baptista-Pike) was conducted for WT and mutant parasites;
1021 'n' denotes the number of parasites analyzed. Individual biological replicates (bioreps) are
1022 displayed, and these data were aggregated and presented in Fig. 5f.